

Towards Zero-Shot Point Cloud Registration Across Diverse Scales, Scenes, and Sensor Setups

Hyungtae Lim* *Member, IEEE*, Minkyun Seo* *Student Member, IEEE*,
 Luca Carloni *Senior Member, IEEE*, and Jaesik Park†, *Member, IEEE*

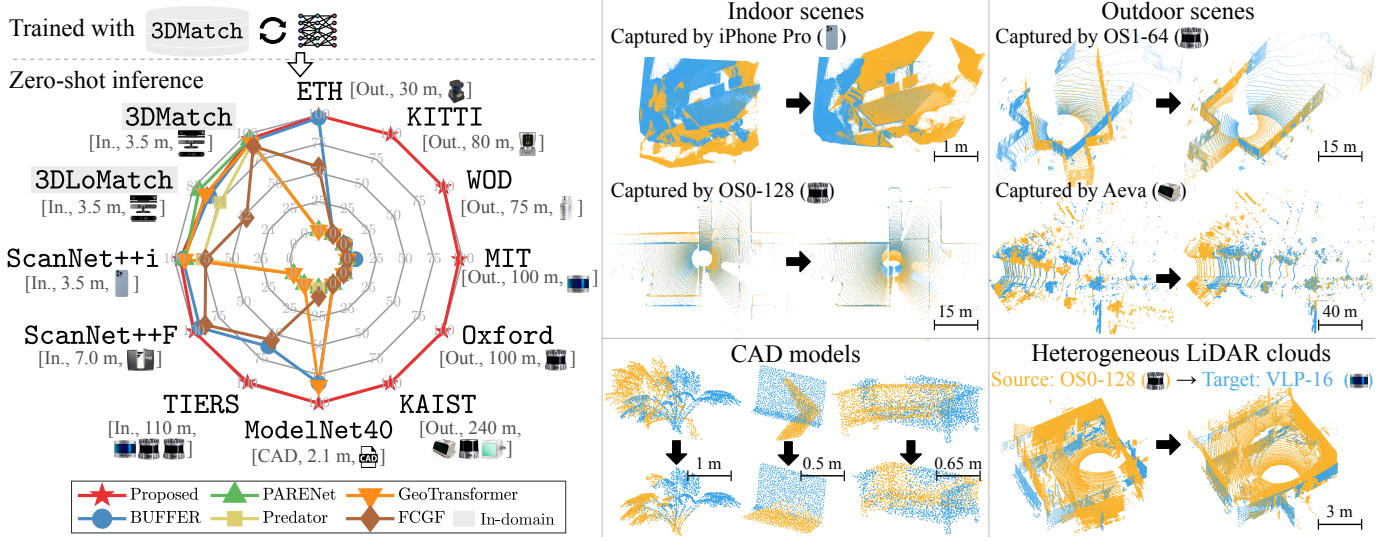


Fig. 1: Success rate (unit: %) of zero-shot point cloud registration with state-of-the-art approaches on 12 datasets [1]–[11]. Without any prior information or manual parameter tuning for the test datasets, our *BUFFER-X* shows robust generalization capability across diverse scales, scenes, and sensor setups even though the network is only trained on the 3DMatch dataset [2]. In particular, our proposed approach can operate on CAD models (from left to right, the point clouds represent a plant, a laptop, and a sofa, respectively) as well as on heterogeneous LiDAR point clouds.

Abstract—Some deep learning-based point cloud registration methods struggle with zero-shot generalization, often requiring dataset-specific hyperparameter tuning or retraining for new environments. We identify three critical limitations: (a) fixed user-defined parameters (e.g., voxel size, search radius) that fail to generalize across varying scales, (b) learned keypoint detectors exhibit poor cross-domain transferability, and (c) absolute coordinates amplify scale mismatches between datasets. To address these three issues, we present *BUFFER-X*, a training-free registration framework that achieves zero-shot generalization through: (a) geometric bootstrapping for automatic hyperparameter estimation, (b) distribution-aware farthest point sampling to replace learned detectors, and (c) patch-level coordinate normalization to ensure scale consistency. Our approach employs hierarchical multi-scale matching to extract correspondences across local, middle, and global receptive fields, enabling robust registration in diverse environments. For efficiency-critical applications, we introduce *BUFFER-X-Lite*, which reduces total computation time by 43% (relative to *BUFFER-X*) through early exit strategies and fast pose solvers while preserving accuracy. We evaluate

on a comprehensive benchmark comprising 12 datasets spanning object-scale, indoor, and outdoor scenes, including cross-sensor registration between heterogeneous LiDAR configurations. Results demonstrate that our approach generalizes effectively without manual tuning or prior knowledge of test domains. Code: <https://github.com/MIT-SPARK/BUFFER-X>.

Index Terms—Point cloud registration, 3D computer vision, Zero-shot registration, Representation learning.

I. INTRODUCTION

DEEP learning methods for point cloud registration have advanced significantly, with improvements spanning feature learning [3], [12]–[18], correspondence matching [3], [19]–[25], and pose solver design [26]–[29]. These methods demonstrate strong in-domain performance, accurately aligning partially overlapping point clouds when evaluated on their training distributions [30]–[35].

However, the ability to generalize across diverse real-world environments remains a key challenge [14], [15], [36]–[38], with recent work focusing on cross-domain transferability. Despite progress in generalization [39], [40], practical deployment of some methods still depends on dataset-specific hyperparameters, particularly voxel size for downsampling and search radius for feature extraction, which must be manually tuned for each new environment. The need for such intervention limits practical applicability, motivating the development

†Corresponding author.

*These authors contributed equally to this work.

Hyungtae Lim and Luca Carloni are with the Laboratory for Information and Decision Systems (LIDS), Massachusetts Institute of Technology, Cambridge, MA, USA (e-mail: {shapelim, lcarloni}@mit.edu)

Minkyun Seo and Jaesik Park are with Department of Computer Science and Engineering, Seoul National University, Seoul, Republic of Korea, (e-mail: {funboy0804, jaesik.park}@snu.ac.kr)

This work has been submitted to the IEEE for possible publication. Copyright may be transferred without notice, after which this version may no longer be accessible.

of truly zero-shot registration methods that operate without manual parameter adjustment.

Additionally, evaluation protocols have historically focused on narrow scenarios: outdoor LiDAR scans [4], [41] or indoor RGB-D data [2]. Cross-domain evaluations involving object-level CAD models [1], indoor LiDAR [6], diverse outdoor scanning patterns [6], [11], [42], or heterogeneous sensor configurations where source and target are captured by different devices, remain underexplored. Therefore, a comprehensive benchmark reflecting real-world sensor diversity is needed to rigorously assess cross-domain generalization.

To address these limitations, this paper builds upon our prior work, *BUFFER-X* [43], and makes two primary contributions: (a) a training-free zero-shot registration framework and (b) a rigorous evaluation benchmark for assessing cross-domain generalization. First, we revisit the zero-shot registration setting and systematically identify three architectural factors that limit zero-shot capability in Sec. III. Based on these insights, we present *BUFFER-X* [43], which employs: (i) geometric bootstrapping to automatically estimate voxel size and search radius per scene, (ii) distribution-aware sampling to replace learned keypoint detectors, and (iii) hierarchical multi-scale patch-based matching for robust correspondence extraction across varying receptive fields. As an extension, to reduce computational cost while maintaining accuracy, we introduce this with *BUFFER-X-Lite*, an efficient variant that achieves 43% reduction in total pipeline time by combining early exit strategies with fast pose solvers.

Second, we extend the evaluation scope of the previous work [43], which was limited to indoor and outdoor scenes captured with homogeneous sensor configurations. In contrast, the expanded evaluation now spans 12 datasets covering object-scale, indoor, and outdoor scenarios, and additionally incorporates object-level CAD models as well as heterogeneous LiDAR registration settings in which the source and target point clouds are acquired using different sensor types. This extension enables a more comprehensive assessment of generalization across scale, data modality, and sensor heterogeneity. Consequently, our experiments demonstrate that *BUFFER-X* generalizes effectively without manual tuning or prior domain knowledge; see Fig. 1.

In summary, this paper extends our previous work with three main directions. First, we expand the benchmark to include object-scale scenes and heterogeneous sensor configurations, enabling broader evaluation of cross-domain generalization (see Secs. VI-A and VII-B). Second, we provide deeper analyses of multi-scale patch-based representations, supported by additional visualizations and quantitative statistics, to clarify their role in improving robustness and generalization capability (see Sec. VII-C). Third, we introduce *BUFFER-X-Lite*, an efficient variant of the original pipeline that substantially reduces computational cost while maintaining comparable performance (see Secs. V and VII-D). In addition, we plan to further invest in open-source development, including simplified installation via tighter integration with Open3D and ROS-compatible packages, to improve usability and facilitate broader adoption by the community.

II. RELATED WORK

3D point cloud registration, which estimates the relative pose between two partially overlapping point clouds, is a fundamental problem in the fields of robotics and computer vision [44]–[48]. Overall, point cloud registration methods are classified into two categories based on whether their performance relies on the availability of an initial guess for registration: a) *local* registration [49]–[54] and b) *global* registration [29]–[34], [55]–[57]. Global registration methods can be further classified into two types: a) *correspondence-free* [34], [58]–[67] and b) *correspondence-based* [24], [25], [29], [33], [40], [55], [56], [68]–[70] approaches. In this study, we focus on the latter and particularly place more emphasis on deep learning-based registration methods.

Since Qi *et al.* [71] demonstrated that learning-based techniques in 2D images can also be applied to 3D point clouds, a wide range of learning-based point cloud registration approaches have been proposed. Building on these advances, novel network architectures with increased capacity have continuously emerged, ranging from MinkUNet [72]–[74], cylindrical convolutional network [14], [15], [75], KPConv [3], [76], [77] to Transformers [16], [78]–[81].

While these advancements have led to improved registration performance, some of these methods often exhibit limited generalization capability, leading to performance degradation when applied to point clouds captured by different sensor configurations or in unseen environments. To tackle the generalization problem, Ao *et al.* [15], [82] introduce SpinNet, a patch-based method that normalizes the range of local point coordinates within a fixed-radius neighborhood to $[-1, 1]$. This demonstrates that patch-wise scale normalization is key to achieving a data-agnostic registration pipeline.

Further, Ao *et al.* [14] proposed *BUFFER* to enhance efficiency by combining point-wise feature extraction with patch-wise descriptor generation. However, we found that such learning-based keypoint detectors can hinder robust generalization, as their failure on out-of-domain distributions may trigger cascading failures in subsequent steps; see Sec. III-B3. In addition, despite the high generalizability of *BUFFER*, we observed that during cross-domain testing, users had to manually specify the optimal voxel size for the test data, which hinders fully zero-shot inference. On the other hand, Wang *et al.* [39] and Zheng *et al.* [40] proposed zero-shot registration approaches that rely heavily on depth images and RGB images, respectively. However, this dependency limits their applicability to diverse point cloud registration scenarios, ranging from object-level CAD models to outdoor environments.

Beyond generalizing across diverse scenes captured by a single sensor type, recent works [6], [11], [83] have broadened the notion of generalizability to heterogeneous sensor configurations, where source and target clouds are captured by different sensor modalities and scanning patterns. Accordingly, evaluating generalizability in point cloud registration requires considering scenarios where the source and target point clouds are obtained from different heterogeneous sensors (*e.g.*, sparse omnidirectional to dense omnidirectional, or omnidirectional

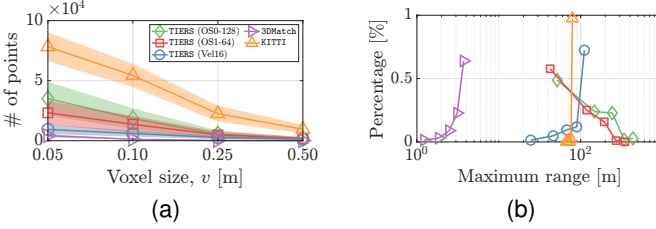


Fig. 2: (a) Variation in the number of points after voxelization with different voxel sizes v across datasets. Even in indoor scenes, point counts vary significantly depending on the sensor type (*i.e.*, TIERS [6] vs. 3DMatch [2]). Notably, TIERS and KITTI [4], both using omnidirectional LiDARs, yield different point densities due to indoor vs. outdoor environments. (b) Empirical distribution of the datasets' maximum range.

to face-forward solid-state LiDAR sensors).

Under these circumstances, we revisit the generalization problem in point cloud registration and explore how to achieve zero-shot registration while preserving the key benefits of BUFFER's scale normalization strategy. In addition, we remove certain modules that hinder robustness and introduce an adaptive mechanism that determines the voxel size and search radii depending on the given point cloud pair. To the best of our knowledge, this is the first approach to evaluate the zero-shot generalization across diverse scenes covering various environments, geographic regions, scales, sensor types, and acquisition setups.

III. PRELIMINARIES

A. Problem statement

The goal of point cloud registration is to estimate the relative 3D rotation matrix $\mathbf{R} \in \text{SO}(3)$ and translation vector $\mathbf{t} \in \mathbb{R}^3$ between two unordered 3D point clouds \mathcal{P} and \mathcal{Q} . To this end, most approaches [3], [84] follow three steps: a) apply voxel sampling $f_v(\cdot)$ to the point cloud with voxel size v as preprocessing, b) establish associations (or *correspondences*) \mathcal{A} , and c) estimate \mathbf{R} and \mathbf{t} .

Formally, by denoting corresponding points for a correspondence (i, j) in \mathcal{A} as $\mathbf{p}_i \in f_v(\mathcal{P})$ and $\mathbf{q}_j \in f_v(\mathcal{Q})$, respectively, the objective function used for pose estimation can be defined as:

$$\hat{\mathbf{R}}, \hat{\mathbf{t}} = \arg \min_{\mathbf{R} \in \text{SO}(3), \mathbf{t} \in \mathbb{R}^3} \sum_{(i, j) \in \mathcal{A}} \rho\left(\|\mathbf{q}_j - \mathbf{R}\mathbf{p}_i - \mathbf{t}\|_2\right), \quad (1)$$

where $\rho(\cdot)$ represents a robust kernel function that mitigates the effect of spurious correspondences in \mathcal{A} .

B. Key observations

If \mathcal{A} in (1) is accurate, solving (1) is a well-studied problem. However, we have observed that there exist three factors that cause learning-based registration to struggle in estimating \mathcal{A} when given out-of-domain data.

1) *Voxel size and search radius*: First, the dependencies of optimal search radius r for local descriptors and voxel size v for each dataset are problematic. The optimal parameters vary significantly across datasets due to differences in scale and point density (*e.g.*, small indoor scenes vs. large outdoor spaces [14]). Consequently, improper r or v can severely degrade registration performance by failing to account for specific scale and density characteristics of a given environment or sensor; see Sec. VII-A. For instance, in Fig. 2(a), as v controls the maximum number of points that can be fed into the network, a too-small v can trigger out-of-memory errors when outdoor data processed with parameters optimized for indoor environments are taken as input to the network.

In particular, most methods heavily depend on manual tuning, which hinders generalization. Therefore, we employ a *geometric bootstrapping* to adaptively determine v and r at test time based on the scale and point density of the given input clouds; see Sec. IV-A.

2) *Input scale normalization*: Next, directly feeding raw x , y , and z values into the network leads to strong in-domain dependency [3], [78]. That is, when a model fits the training distribution, large-scale discrepancies between training and unseen data can cause catastrophic failure (see Fig. 2(b) for an example of maximum range discrepancy). For this reason, we conclude that normalizing input points within local neighborhoods (or *patches*) is necessary to achieve generalizability, ensuring that their coordinates lie within a bounded range (*e.g.*, $[-1, 1]$) [14], [15].

Based on these insights, we adopt patch-based descriptor generation as our pipeline for descriptor matching; see Sec. IV-B.

3) *Keypoint detection*: Following Sec. III-B2, we observed that point-wise feature extractor modules in existing methods [3], [78], [85] are empirically brittle to out-of-domain data. Because failed keypoint detection leads to the selection of unreliable and non-repeatable points as keypoints, it results in low-quality descriptors and ultimately degrades the quality of \mathcal{A} [86].

An interesting observation is that replacing the learning-based detector with farthest point sampling (FPS) preserves registration performance [43]. For this reason, we adopt FPS over a learning-based module. Specifically, we apply it separately at local, middle, and global scales to account for multi-scale variations.

IV. BUFFER-X

Building upon our key observations in Sec. III-B, we present our multi-scale zero-shot registration pipeline; see Fig. 3. First, the appropriate voxel size and radii for each cloud pair are predicted by geometric bootstrapping (Sec. IV-A), considering the overall distribution of cloud points and the density of neighboring points, respectively. Then, we extract Mini-SpinNet-based features [14] for the sampled points via FPS at multiple scales (Sec. IV-B). Finally, at the intra- and cross-scale levels, refined correspondences are estimated based on consensus maximization [26], [87], [88] (Sec. IV-C) and serve as input for the final relative pose estimation using a solver.

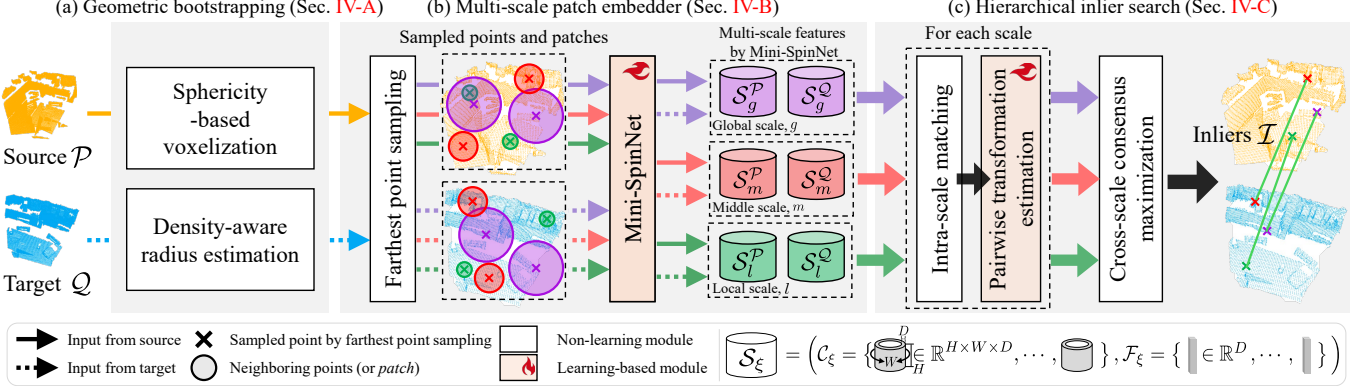


Fig. 3: Overview of our *BUFFER-X*, which mainly consists of three steps. (a) Geometric bootstrapping (Sec. IV-A) to determine the appropriate voxel size and radii for the given source \mathcal{P} and target \mathcal{Q} clouds. (b) Multi-scale patch embedder (Sec. IV-B) to generate patch-wise descriptor \mathcal{S}_ξ for multiple scales $\xi \in \{l, m, g\}$, where l , m , and g represent local, middle, and global scales, respectively. Specifically, Mini-SpinNet [14] outputs cylindrical feature maps \mathcal{C}_ξ and vector feature sets \mathcal{F}_ξ . (c) Hierarchical inlier search (Sec. IV-C), which first performs nearest neighbor-based intra-scale matching using \mathcal{F}_ξ^P and \mathcal{F}_ξ^Q at each scale, followed by pairwise transformation estimation. Finally, it identifies globally consistent inliers \mathcal{I} across all scales to refine correspondences based on consensus maximization [87], [88].

A. Geometric bootstrapping

Sphericity-based voxelization. First, we determine a suitable voxel size v by leveraging sphericity, quantified using eigenvalues [89], [90], to reflect the spatial dispersion of point clouds. To this end, we apply principal component analysis (PCA) [91] to the covariance of sampled points, which can efficiently capture point dispersion by analyzing eigenvalues while remaining computationally lightweight.

Formally, let $h(\mathcal{P}, \mathcal{Q})$ be a function that selects the largest point cloud based on cardinality, let $g(\mathcal{P}, \delta)$ be a function that samples $\delta\%$ of points from a given point cloud, and let $\mathbf{C} \in \mathbb{R}^{3 \times 3}$ be the covariance of $g(h(\mathcal{P}, \mathcal{Q}), \delta_v)$, where δ_v is a user-defined sampling ratio. Then, using PCA, three eigenvalues λ_a and their corresponding eigenvectors \mathbf{v}_a are calculated as follows:

$$\mathbf{C}\mathbf{v}_a = \lambda_a \mathbf{v}_a, \quad a \in \{1, 2, 3\}, \quad (2)$$

which are assumed to be $\lambda_1 \geq \lambda_2 \geq \lambda_3$. Then, using these properties, we can compute the *sphericity* $\frac{\lambda_3}{\lambda_1}$ [90], which quantifies how evenly a point cloud is distributed in space. Since LiDAR points are primarily distributed along the sensor's horizontal plane (*i.e.*, forming a disc-like shape), $\frac{\lambda_3}{\lambda_1}$ tends to be low compared to RGB-D point clouds.

In addition, as observed in Fig. 2(a), LiDAR point clouds require a larger voxel size; thus, we set v as follows:

$$v = \begin{cases} \kappa_{\text{spheric}} \sqrt{s}, & \text{if } \frac{\lambda_3}{\lambda_1} \geq \tau_v, \\ \kappa_{\text{disc}} \sqrt{s}, & \text{otherwise,} \end{cases} \quad (3)$$

where κ_{spheric} and κ_{disc} are constant user-defined coefficients across all datasets, satisfying $\kappa_{\text{spheric}} < \kappa_{\text{disc}}$, τ_v is a user-defined threshold, and s is the length that represents the spread of points along the eigenvector corresponding to the smallest eigenvalue \mathbf{v}_3 (*i.e.*, $s = \max(\mathcal{P}_{\text{sampled}} \cdot \mathbf{v}_3) - \min(\mathcal{P}_{\text{sampled}} \cdot \mathbf{v}_3)$). Consequently, as $\frac{\lambda_3}{\lambda_1}$ and s adapt based on the environment (*i.e.*, indoor or outdoor) and the field of view of the sensor type (*i.e.*, RGB-D or LiDAR point cloud), (3) enables the adaptive

setting of v .

Hereafter, for brevity, we denote $f_v(\mathcal{P})$ and $f_v(\mathcal{Q})$ simply as \mathcal{P} and \mathcal{Q} , respectively,

Density-aware radius estimation. Next, in contrast to some state-of-the-art approaches [14], [15] that use a single fixed user-defined search radius, we determine r at local, middle, and global scales, respectively, by considering the input point densities. Let neighboring search function within the radius r around a query point \mathbf{p}_q be:

$$\mathcal{N}(\mathbf{p}_q, \mathcal{P}, r) = \{\mathbf{p} \in \mathcal{P} \mid \|\mathbf{p} - \mathbf{p}_q\|_2 \leq r\}. \quad (4)$$

Then, as presented in Fig. 4(a), the radius for patch-wise descriptor generation for each scale r_ξ is defined as follows:

$$r_\xi = \arg \min_r \left| \frac{1}{N} \sum_{\mathbf{p}_q \in \mathcal{P}_r} \text{card}(\mathcal{N}(\mathbf{p}_q, \mathcal{P}_r, r)) - \tau_\xi \right|, \quad (5)$$

where $\xi \in \{l, m, g\}$ denotes the scale level (*i.e.*, local, middle, and global scale, respectively), τ_ξ denotes the user-defined threshold, which represents the desired neighborhood density (*i.e.*, average proportion of neighboring points relative to the total number of points), satisfying $\tau_l \leq \tau_m \leq \tau_g$ (accordingly, $r_l \leq r_m \leq r_g$ as presented in Fig. 4(a)), and \mathcal{P}_r is a set of N_r points sampled from $h(\mathcal{P}, \mathcal{Q})$, where N_r is a user-defined parameter for radius estimation. To account for cases where the points are too sparse, we set the maximum truncation radius r_{\max} as $r_\xi \leftarrow \max(r_\xi, r_{\max})$.

B. Multi-scale patch embedder

Next, with the voxelized point clouds \mathcal{P} and \mathcal{Q} and radii estimated by (5), patch-wise descriptors are generated at each scale.

Farthest point sampling. As discussed in Sec. III-B3, we sample \mathcal{P}_ξ from \mathcal{P} at each scale using FPS to be free from a learning-based keypoint detector (resp. \mathcal{Q}_ξ from \mathcal{Q}). Note that

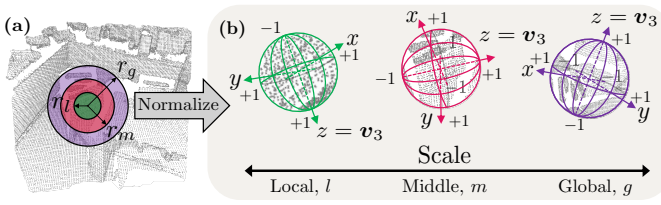


Fig. 4: (a) Visual description of local (r_l), middle (r_m), and global (r_g) radii for the same point to illustrate scale differences and (b) normalized patches ranging from $[-1, 1]$. Note that their reference frames follow the eigenvectors obtained from principal component analysis (PCA) [90], [91]. The z -axis is assigned to the eigenvector \mathbf{v}_3 , which corresponds to the smallest eigenvalue.

instead of extracting local, middle, and global-scale descriptors for the same sampled point [92], we independently sample separate points for each scale, as illustrated in Fig. 3(b). This is because we empirically found that different regions may require distinct scales for optimal feature extraction [43].

Mini-SpinNet-based descriptor generation. Using multiple radii r_ξ , we sample patches at three distinct scales, providing a more comprehensive multi-scale representation. Then, we use Mini-SpinNet [14] for descriptor generation, which is a lightweight version of SpinNet [15].

In particular, building on the insights from Sec. III-B2, we ensure the scale of points in each patch is normalized to a bounded range of $[-1, 1]$ by dividing by r_ξ ; see Fig. 4(b). By doing so, we can resolve the dependency on the training domain scale. To maintain consistency across patches at all scales, we fix the patch size to N_{patch} and randomly sample when a patch exceeds this size, ensuring a consistent number of points regardless of scale variations.

Finally, taking these normalized patches as inputs, Mini-SpinNet outputs a superset \mathcal{S}_ξ^P consisting of D -dimensional feature vectors \mathcal{F}_ξ^P and cylindrical feature maps \mathcal{C}_ξ^P , which corresponds to \mathcal{P}_ξ (resp. \mathcal{S}_ξ^Q consisting of \mathcal{F}_ξ^Q and \mathcal{C}_ξ^Q from \mathcal{Q}_ξ), as described in Fig. 3. Note that while BUFFER [14] utilizes learned reference axes to extract cylindrical coordinates, our approach defines the reference axes for each patch by applying PCA to the covariance of points within the patch, setting the z -direction as \mathbf{v}_3 (as in (2) and illustrated by $z = \mathbf{v}_3$ in Fig. 4(b)), to eliminate potential dataset-specific inductive biases.

C. Hierarchical inlier search

Here, we first perform intra-scale matching to get initial correspondences \mathcal{A}_ξ at each scale and then establish cross-scale consistent correspondences in a consensus maximization manner.

Intra-scale matching. First, we perform nearest neighbor-based mutual matching [93] between \mathcal{F}_ξ^P and \mathcal{F}_ξ^Q , yielding matched correspondences \mathcal{A}_ξ at each scale. Using \mathcal{A}_ξ , we extract the corresponding elements from \mathcal{C}_ξ^P and \mathcal{C}_ξ^Q , denoted as $\widehat{\mathcal{C}}_\xi^P$ and $\widehat{\mathcal{C}}_\xi^Q$, and the sampled keypoints from \mathcal{P}_ξ and \mathcal{Q}_ξ as

$\widehat{\mathcal{P}}_\xi$ and $\widehat{\mathcal{Q}}_\xi$, respectively (i.e., $|\mathcal{A}_\xi| = |\widehat{\mathcal{C}}_\xi^P| = |\widehat{\mathcal{C}}_\xi^Q| = |\widehat{\mathcal{P}}_\xi| = |\widehat{\mathcal{Q}}_\xi|$).

Pairwise transformation estimation. Next, using each cylindrical feature pair $\mathbf{c}^P \in \widehat{\mathcal{C}}_\xi^P$ and $\mathbf{c}^Q \in \widehat{\mathcal{C}}_\xi^Q$ at each scale, each of size $\mathbb{R}^{H \times W \times D}$, we calculate pairwise 3D relative transformation between two patches. Here, H , W , and D denote the height, sector size for the yaw direction along the z -axis of the reference axes, and feature dimensionality of a cylindrical feature, respectively; see Fig. 3.

As mentioned in Fig. 4(b), since the cylindrical feature is aligned with the local reference axes via PCA, we estimate the relative 3D rotation by first computing the rotation between the patch-wise principal direction \mathbf{v}_3^P (resp. \mathbf{v}_3^Q) and the global z -axis of the point cloud coordinate frame, $\mathbf{z} = [0 \ 0 \ 1]^\top$, following Ao *et al.* [14]. Specifically, using Rodrigues' rotation formula [94], the rotation matrix is given by:

$$\mathbf{R}^P = \mathbf{I} + \sin(\theta^P)[\mathbf{n}^P]_\times + (1 - \cos(\theta^P))[\mathbf{n}^P]_\times^2, \quad (6)$$

where $\mathbf{n}^P = \mathbf{v}_3^P \times \mathbf{z}$, $\theta^P = \cos^{-1}(\mathbf{v}_3^P \cdot \mathbf{z})$, and $[\cdot]_\times$ denotes the skew operator (resp. \mathbf{R}^Q). Thus, once the yaw rotation between the two patches \mathbf{R}_{yaw} is determined, the full 3D rotation can be obtained as $\mathbf{R} = (\mathbf{R}^Q)^\top \mathbf{R}_{\text{yaw}} \mathbf{R}^P$.

As explained by Ao *et al.* [14], \mathbf{c}^P and \mathbf{c}^Q follow discretized SO(2)-equivariant representation; thus, by finding the yaw rotation that maximizes circular cross-correlation between \mathbf{c}^P and \mathbf{c}^Q , we can estimate the relative SO(2) rotation \mathbf{R}_{yaw} . To this end, a 4D matching cost volume $\mathbf{V} \in \mathbb{R}^{H \times W \times \bar{W} \times D}$ is constructed to represent the sector-wise differences between \mathbf{c}^P and \mathbf{c}^Q . Then, \mathbf{V} is processed by a 3D cylindrical convolutional network (3DCCN) [15], mapping \mathbf{V} to a score vector β of size \bar{W} .

By applying the softmax operation $\sigma(\cdot)$ to β , we obtain $\sigma(\beta)$, where the w -th element $\sigma_w(\beta) \in [0, 1]$ represents the probability mass assigned to the discrete yaw rotation index w . Using this distribution, the expected rotation offset d is computed as follows:

$$d = \sum_{w=1}^{\bar{W}} \sigma_w(\beta) \times w. \quad (7)$$

Finally, \mathbf{R}_{yaw} is calculated as follows:

$$\mathbf{R}_{\text{yaw}} = \begin{bmatrix} \cos\left(\frac{2\pi d}{\bar{W}}\right) & -\sin\left(\frac{2\pi d}{\bar{W}}\right) & 0 \\ \sin\left(\frac{2\pi d}{\bar{W}}\right) & \cos\left(\frac{2\pi d}{\bar{W}}\right) & 0 \\ 0 & 0 & 1 \end{bmatrix}. \quad (8)$$

Subsequently, the translation vector is given by $\mathbf{t} = \mathbf{q} - \mathbf{R}\mathbf{p}$, where $\mathbf{p} \in \widehat{\mathcal{P}}_\xi$ and $\mathbf{q} \in \widehat{\mathcal{Q}}_\xi$ are a matched point pair.

Cross-scale consensus maximization. Then, using per-pair (\mathbf{R}, \mathbf{t}) estimates from all scales, the 3D point pairs with the largest cardinality across scales should be selected as the final inlier correspondences \mathcal{I} , ensuring cross-scale consistency. To achieve this, we formulate the cross-scale inlier selection as *consensus maximization* problem [87], [88].

Formally, by denoting $N = \sum_\xi |\mathcal{A}_\xi|$, let $(\mathbf{R}, \mathbf{t}) \in \mathcal{T}$ be a candidate transformation set of size N , and let $(\mathbf{p}_n, \mathbf{q}_n) \in \mathcal{D}$ be the set of matched point pairs, where $n \in \{1, \dots, N\}$,

Algorithm 1: BUFFER-X pipeline

```

1 Input: Source cloud  $\mathcal{P}$  and target cloud  $\mathcal{Q}$ ; User-defined
   parameters  $\tau_v$ ,  $\delta_v$ ,  $\delta_r$ ,  $[\tau_l, \tau_m, \tau_g]$ , and  $N_{\text{FPS}}$ 
2 Output: 3D inliers  $\mathcal{I}$ 
3  $\mathcal{P}_r \leftarrow \text{select\_larger\_cloud}(\mathcal{P}, \mathcal{Q})$ 
4  $\mathcal{P}_{\text{sampled}} = \text{sample}(\mathcal{P}_r, \delta_v)$  % Sample  $\delta_v\%$  of cloud points
5 % Step 1. Geometric bootstrapping
6  $v = \text{calc\_voxel\_size}(\mathcal{P}_{\text{sampled}}, \tau_v)$  % See Eq. (3)
7  $\mathcal{P} \leftarrow f_v(\mathcal{P}), \mathcal{Q} \leftarrow f_v(\mathcal{Q})$  % Downsample the point clouds
8  $\mathcal{P}_r \leftarrow \text{select\_larger\_cloud}(\mathcal{P}, \mathcal{Q})$ 
9  $\mathcal{R} = \text{estimate\_radii}(\text{sample}(\mathcal{P}_r, N_r), [\tau_l, \tau_m, \tau_g]),$ 
10 where  $\mathcal{R} = [r_l, r_m, r_g]$  % See Eq. (5)
11 % Step 2. Multi-scale patch embedder
12  $\mathcal{M}^{\mathcal{P}} = \emptyset, \mathcal{M}^{\mathcal{Q}} = \emptyset$  % Containers of embedding output
13 for  $r_{\xi}$  in  $\mathcal{R}$  do
14    $\mathcal{P}_{\xi} = \text{farthest\_point\_sampling}(\mathcal{P}, N_{\text{FPS}})$ 
15    $\mathcal{Q}_{\xi} = \text{farthest\_point\_sampling}(\mathcal{Q}, N_{\text{FPS}})$ 
16    $\mathcal{F}_{\xi}^{\mathcal{P}}, \mathcal{C}_{\xi}^{\mathcal{P}} = \text{MiniSpinNet}(\mathcal{P}_{\xi}, \mathcal{P}, r_{\xi})$ 
17    $\mathcal{F}_{\xi}^{\mathcal{Q}}, \mathcal{C}_{\xi}^{\mathcal{Q}} = \text{MiniSpinNet}(\mathcal{Q}_{\xi}, \mathcal{Q}, r_{\xi})$ 
18    $\mathcal{M}^{\mathcal{P}}.\text{append}((\mathcal{P}_{\xi}, \mathcal{F}_{\xi}^{\mathcal{P}}, \mathcal{C}_{\xi}^{\mathcal{P}}))$ 
19    $\mathcal{M}^{\mathcal{Q}}.\text{append}((\mathcal{Q}_{\xi}, \mathcal{F}_{\xi}^{\mathcal{Q}}, \mathcal{C}_{\xi}^{\mathcal{Q}}))$ 
20 end
21 % Step 3. Hierarchical inlier search
22  $\mathcal{D} = \emptyset, \mathcal{T} = \emptyset$ 
23 for  $i$  in range(size( $\mathcal{M}^{\mathcal{P}}$ )) do
24    $(\mathcal{P}_{\xi}, \mathcal{F}_{\xi}^{\mathcal{P}}, \mathcal{C}_{\xi}^{\mathcal{P}}) = \mathcal{M}^{\mathcal{P}}[i]$ 
25    $(\mathcal{Q}_{\xi}, \mathcal{F}_{\xi}^{\mathcal{Q}}, \mathcal{C}_{\xi}^{\mathcal{Q}}) = \mathcal{M}^{\mathcal{Q}}[i]$ 
26   % Step 3-1. Nearest neighbor-based intra-scale matching
27    $\mathcal{A}_{\xi} = \text{mutual\_matching}(\mathcal{F}_{\xi}^{\mathcal{P}}, \mathcal{F}_{\xi}^{\mathcal{Q}})$ 
28    $(\widehat{\mathcal{P}}_{\xi}, \widehat{\mathcal{Q}}_{\xi}, \widehat{\mathcal{C}}_{\xi}^{\mathcal{P}}, \widehat{\mathcal{C}}_{\xi}^{\mathcal{Q}}) = \text{filter}(\mathcal{M}^{\mathcal{P}}[i], \mathcal{M}^{\mathcal{Q}}[i], \mathcal{A}_{\xi})$ 
29   % Step 3-2. Pairwise transformation estimation
30    $\mathcal{T}_{\xi} = \text{calc\_pairwise\_R\_and\_t}(\widehat{\mathcal{C}}_{\xi}^{\mathcal{P}}, \widehat{\mathcal{C}}_{\xi}^{\mathcal{Q}})$ 
31    $\mathcal{D}.\text{append}((\widehat{\mathcal{P}}_{\xi}, \widehat{\mathcal{Q}}_{\xi})), \mathcal{T}.\text{append}(\mathcal{T}_{\xi})$ 
32 end
33 % Step 3-3. Cross-scale consensus maximization
34  $\mathcal{I} = \text{consensus\_maximization}(\mathcal{D}, \mathcal{T})$  % See Eq. (9)

```

$\mathbf{p}_n \in \bigcup_{\xi} \widehat{\mathcal{P}}_{\xi}$ and $\mathbf{q}_n \in \bigcup_{\xi} \widehat{\mathcal{Q}}_{\xi}$. Then, \mathcal{I} is estimated as follows:

$$\begin{aligned} & \max_{(\mathbf{R}, \mathbf{t}) \in \mathcal{T}, \mathcal{I}} |\mathcal{I}| \\ \text{s.t. } & \|\mathbf{R}\mathbf{p}_n + \mathbf{t} - \mathbf{q}_n\|_2 < \epsilon, \quad \forall (\mathbf{p}_n, \mathbf{q}_n) \in \mathcal{I} \subseteq \mathcal{D}, \end{aligned} \quad (9)$$

where ϵ is an inlier threshold. That is, the objective in (9) maximizes the number of inlier correspondences aggregated across multiple scales, and the resulting transformation is estimated using a robust solver such as RANSAC [55] or TEASER++ [30].

Pseudo code of our approach is presented in Algorithm 1.

D. Loss function and training

Loss functions. Unlike BUFFER, which was trained in four stages, our network follows a relatively simpler two-stage training process thanks to its detector-free nature. First, we train the feature discriminability of Mini-SpinNet descriptors using contrastive learning [41], followed by training d in (7) to improve transformation estimation accuracy.

In particular, we employ the Huber loss [95] $\rho_{\text{Huber}}(\cdot)$ for training d while remaining robust to outliers [96], which is formulated as follows:

$$\rho_{\text{Huber}}(r) = \begin{cases} \frac{1}{2}r^2, & \text{if } |r| \leq \delta \\ \delta(|r| - \frac{1}{2}\delta), & \text{otherwise,} \end{cases} \quad (10)$$

where r denotes the residual and δ denotes the user-defined truncation threshold. Then, denoting the total number of data pairs by N_d , the γ -th predicted offset by d_{γ} , and the corresponding ground-truth offset by d_{γ}^* , the loss function \mathcal{L}_d is defined as follows:

$$\mathcal{L}_d = \frac{1}{N_d} \sum_{\gamma=1}^{N_d} \rho_{\text{Huber}}(d_{\gamma} - d_{\gamma}^*). \quad (11)$$

Patch distribution augmentation. Furthermore, we propose an inter-patch point distribution augmentation to allow Mini-SpinNet to experience a wider variety of patch distribution patterns. Specifically, we empirically sample the radius within $[\frac{2}{3}r, \frac{4}{3}r]$ based on a uniform probability. As mentioned in Sec. IV-B, since N_{patch} points within the radius are randomly selected as an input, a diverse set of patterns can be provided as r varies.

Notably, training is conducted using only a single scale. This leverages the scale normalization characteristic of BUFFER-X, making it unnecessary to train with multi-scale separately.

V. BUFFER-X-LITE: REDUCING COMPUTATION TIME

While BUFFER-X achieves strong generalization through multi-scale matching, which is essential for handling diverse registration scenarios, the computational cost can be reduced for certain registration pairs where reliable alignment can be achieved with fewer scales. The key insight is that not all pairs require processing all three scales (*i.e.*, some easier pairs may find sufficient inliers at local or middle scales, while challenging pairs benefit from the full multi-scale hierarchy). To achieve faster inference while preserving this multi-scale robustness, we introduce BUFFER-X-Lite by (i) decreasing the number of scales processed via adaptive early exit when sufficient evidence is found, and (ii) decreasing solver time at each processed scale by replacing RANSAC with a faster graduated non-convexity (GNC) [30]-based pose estimation solver.

A. Strategy 1: Decreasing the number of scales processed

The first strategy reduces computation by adaptively terminating after processing only one scale when sufficient inliers are detected, thereby reducing the total number of feature descriptors that need to be computed. Importantly, this does not claim that a single scale is universally sufficient; rather, it adapts computational effort based on the difficulty of each registration pair, processing additional scales only when needed. After obtaining correspondences at the middle scale, we estimate the initial pose and count the number of inliers. This adaptive early exit approach is inspired by recent advances in image feature matching [97] and robust estimation [98], where similar strategies have proven effective in balancing computation reduction with matching quality.

Formally, we first process only the middle scale (*i.e.*, $\xi = m$) to obtain inliers \mathcal{I}_m through the matching procedure described through Sec. III-B1 and Sec. IV-C. If $|\mathcal{I}_m|$ exceeds a user-defined threshold τ_N , we terminate early and skip the local and global scales entirely, as sufficient consensus

has been found for reliable registration. Lower values of τ_N enable more aggressive early exit (processing fewer scales on average), while higher values ensure more robust registration by processing additional scales more frequently. Otherwise, we proceed with the full three-scale pipeline as in standard BUFFER-X with an efficient solver presented in Sec. V-B.

B. Strategy 2: Decreasing solver time

The second strategy reduces the pose estimation time at each scale by replacing RANSAC with a faster solver [84]. While RANSAC also employs an early exit concept, in the worst case, traditional RANSAC requires numerous random sampling iterations (*e.g.*, 50K iterations in our experiments) to achieve reliable registration. Empirically, for noisy point cloud pairs, this takes approximately 0.1 sec on an AMD Ryzen Threadripper 7960X 24-Core processor, which is non-negligible and accumulates with multi-stage pose estimation. To reduce this solver time, we employ deterministic graph-theoretic k -core pruning [98] followed by a GNC solver [99], instead of iterative random sampling. This approach is proposed in our previous work, KISS-Matcher [84], whose solver component we refer to as *KISS-Matcher solver*.

Specifically, KISS-Matcher solver first constructs a compatibility graph $\mathcal{G}(\mathcal{V}, \mathcal{E})$ where vertices represent correspondences and edges connect pairs satisfying the geometric consistency constraint:

$$-2\beta \leq \|\mathbf{q}_j - \mathbf{q}_{j'}\| - \|\mathbf{p}_i - \mathbf{p}_{i'}\| \leq 2\beta \quad (12)$$

for correspondences $(\mathbf{p}_i, \mathbf{q}_j)$ and $(\mathbf{p}_{i'}, \mathbf{q}_{j'})$, where $\beta = 1.5v$ is the inlier noise bound. The maximum k -core of this graph forms a candidate inlier set in linear time $O(|\mathcal{V}| + |\mathcal{E}|)$, which is then refined by a GNC solver. In contrast, RANSAC requires $O(N_{\text{iter}} \cdot |\mathcal{V}|)$ complexity, where N_{iter} denotes the number of iterations (typically 50K in our experiments). This substantial reduction in computational complexity makes KISS-Matcher solver particularly beneficial when combined with early exit, enabling rapid evaluation of whether sufficient inliers have been found for reliable registration.

C. Combined effect: Faster and reliable inference

The combination of these two strategies enables both computational efficiency and reliable decision-making. The early exit mechanism adaptively processes additional scales only when needed, while KISS-Matcher solver ensures efficient pose estimation with reliable inlier detection.

Critically, successful early exit requires accurately determining when sufficient evidence has been found to be considered as successful registration versus when additional scales are necessary. Interestingly, KISS-Matcher solver produces well-separated inlier distributions compared to RANSAC, making the final inliers easily discernible. This clear separation enables confident early termination decisions, maximizing correct early exits while minimizing premature termination; see Sec. VII-D.

VI. EXPERIMENT SETUPS

A. Datasets for generalizability benchmark

We designed our generalizability benchmark using twelve datasets [1]–[11] as follows. Quantitative analyses can be found in Fig. 5.

- ModelNet40 follows conventional protocol used in 3D CAD registration benchmark [1]. Note that the scale of ModelNet40 is up to 15 \times smaller than those in outdoor sequences (see Figs. 5(a) and (b)).
- 3DMatch follows the conventional protocol proposed by Zeng *et al.* [2].
- 3DLoMatch follows the conventional protocol proposed by Huang *et al.* [3]. This dataset is derived from 3DMatch by selectively extracting pairs with low overlap (*i.e.*, 10–30%), allowing for the evaluation of robustness to low-overlap scenarios.
- ScanNet++i is from ScanNet++ [5]. There are depth images captured using a LiDAR sensor attached to an iPhone 13 Pro. These depth images were converted into point clouds using the toolbox provided by 3DMatch [2]. To generate dense point cloud fragments, 50 consecutive frames were accumulated. Finally, pairs with an overlap ratio of at least 0.4 (*i.e.*, 40% overlap between two fragments) were selected as the final test pairs.
- ScanNet++F is also from ScanNet++ [5]. Since the dataset provides only a merged PLY map and stationary FARO LiDAR poses, but no individual scans, we generate virtual scans by raycasting from each pose into the merged point cloud. The ray sampling follows the scanner’s horizontal and vertical angular resolutions [100], and the nearest intersection along each ray is selected to simulate realistic scans.
- TIERS consists of Indoor06, Indoor08, Indoor09, Indoor10, and Indoor11 sequences in the TIERS dataset [6], as presented in Fig. 6(a). In particular, we used data obtained from the Velodyne VLP-16, Ouster OS1-64, and Ouster OS0-128. Although additional sensors are available, point clouds from the Livox Horizon and Livox Avia can contain too few points or capture only partial wall surfaces, which are not suitable for registration evaluation.
- ETH is from the gazebo_summer, gazebo_winter, wood_autumn, and wood_summer sequences of the dataset proposed by Pomerleau *et al.* [10]. The original dataset contains a wider variety of scenes; however, following the existing protocol proposed by Ao *et al.* [14], we used four sequences.
- KITTI follows the conventional protocol proposed by Yew *et al.* [41]. In test scenes, 08, 09, and 10 sequences are employed.
- MIT is from 10_14_acl_jackal sequence of the Kimera-Multi dataset [9], which is acquired using a Velodyne VLP 16 sensor on the MIT campus. We refer to a subset of it as MIT in our paper to highlight that our dataset was curated with consideration for geographic and cultural environments. Similarly, we use Oxford (from the NewerCollege dataset [7]) and KAIST (from the

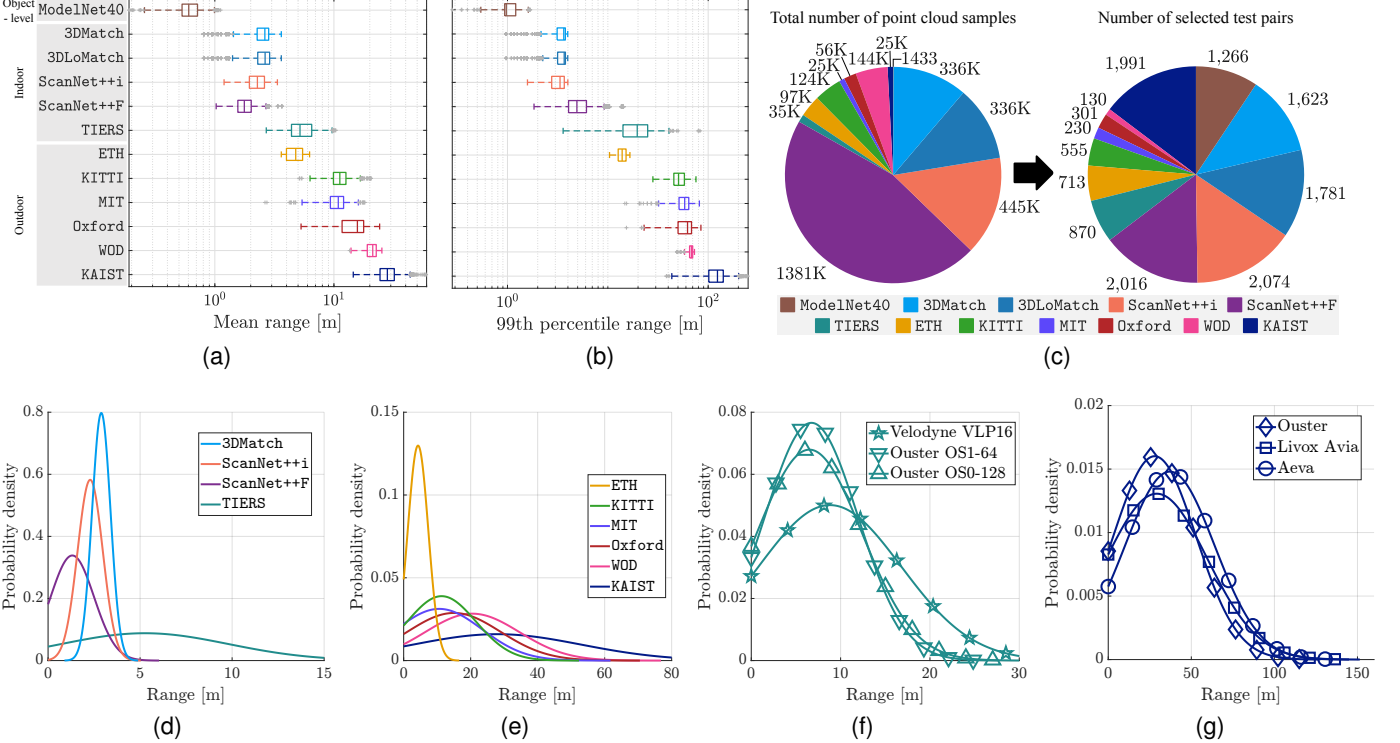


Fig. 5: Dataset statistics and characteristics analysis, which demonstrates the diversity of point cloud characteristics across different environments, sensor types, and acquisition scenarios in our generalizability benchmark. (a)-(b) Box plots of mean and 99th percentile range per frame across different datasets, respectively. (c) Distribution of the number of point clouds and the number of selected test pairs across indoor and outdoor environments. (d)-(e) Gaussian distribution of ranges for indoor and outdoor scenes, respectively, and (f)-(g) those for different sensor types in the TIERS and KAIST sequences.

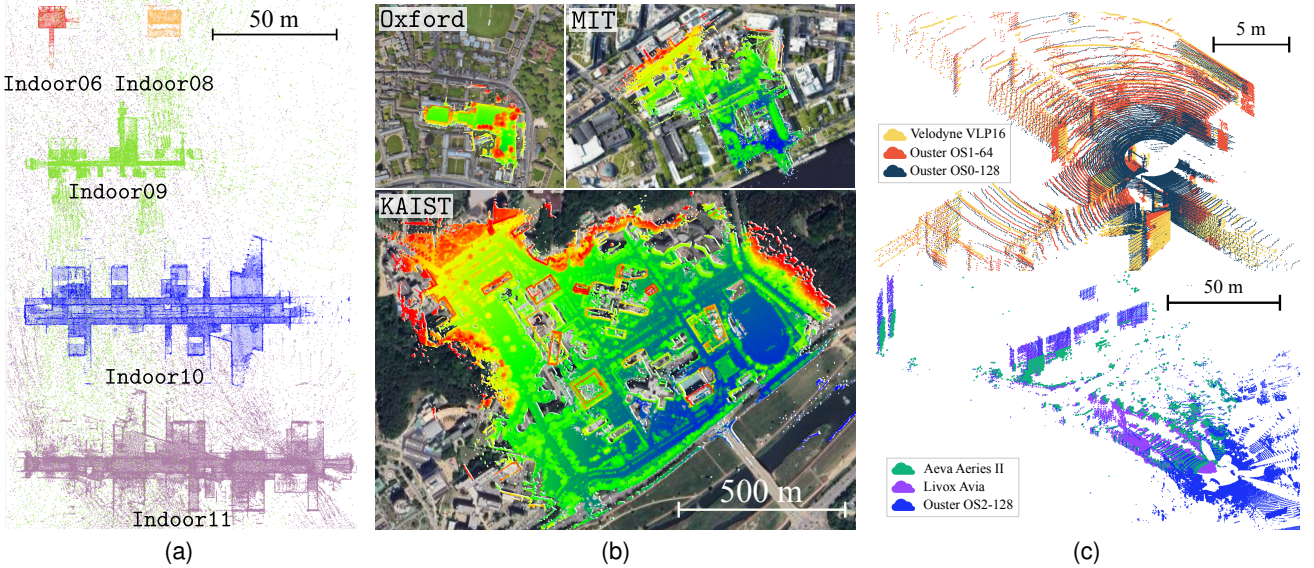


Fig. 6: (a) Different scales of sequences from the TIERS dataset [6] in our experiments. While each scan is utilized for our evaluation, we build and then visualize map clouds using LiDAR point cloud scans and corresponding poses to illustrate the different scales of the surroundings. (b) Scale comparison of three sequences: Oxford from the NewerCollege dataset [7], MIT from Kimera-Multi [9], and KAIST from the HeLiPR dataset [11] at the same scale (*i.e.*, 500 m). Note that although these sequences fall under the same campus category, their scales differ. For clarity, the map clouds are visualized with respect to their z values. (c) (T-B) Examples of visualized LiDAR scans from different LiDAR sensors in the Indoor10 of TIERS dataset [6] and KAIST05 sequence of the HeLiPR dataset [11]. Note that even in the same environment, differences in the number of LiDAR rays and the field of view result in point clouds with different patterns.

HeLiPR dataset [11]) to emphasize the institutions for the same reason.

- Oxford is from the 01, 05, and 07 sequences of the NewerCollege dataset [7]. An interesting aspect is that 01 and 07 were acquired by a handheld setup, while the 05 sequence was acquired using a quadruped robot. As shown in Fig. 6(b), the campus scale was relatively small, so if we use only a single sequence, it only generates few test pairs. For that reason, to ensure at least a similar number of test pairs as MIT, we used three sequences.
- WOD follows the protocol proposed by Liu *et al.* [25]. This dataset is from the Waymo Open Dataset [8] Perception dataset by extracting LiDAR sequences and corresponding pose files.
- KAIST is from the KAIST05 sequence of the HeLiPR dataset [11]. Originally, HeLiPR contains multiple sequences, but each sequence in the HeLiPR is much longer than those in MIT and Oxford, resulting in many more test pairs compared to other campus scenes (see Fig. 5(c)). For this reason, we balanced the datasets by using only one sequence.

By using these datasets, we evaluate the registration approaches on four aspects. First, we assess *variation in environmental scales*, ranging from small objects to large indoor and outdoor environments. Unlike our previous work [43] that primarily used indoor and outdoor scenes, we include ModelNet40, which is an object-scale CAD-based point cloud dataset, to challenge the domain shift. Although all TIERS sequences were collected within the same indoor building, they were captured in diverse environments such as rooms, classrooms, and hallways, with significantly varying scales of surroundings. Note that even within indoor or outdoor scenes, variations in scale (or range) are significantly different, as presented in Figs. 5(d), 5(e), 6(a), and 6(b).

Second, we evaluate robustness to *different scanning patterns with different sensor types*. Using KAIST and TIERS, we assess whether the same space remains robust to different scanning patterns, as variations in the number of laser rays and sensor patterns result in different representations (Fig. 6(c)).

Third, we examine *acquisition setups* to evaluate beyond the typical setting where indoor scanning is performed using handheld devices while outdoor scanning is conducted using vehicles. We include TIERS (acquired using a sensor cart), Oxford (acquired using both a handheld device and a quadruped robot), and MIT (captured using a mobile robot with planar motion but significantly more roll and pitch motion compared to a vehicle).

Fourth, we assess *diversity of geographic and cultural environments*. That is, we leveraged datasets collected by different teams from campuses in Asia, Europe, and the USA to evaluate whether such geographic and cultural variations have an impact on performance.

Training settings. To evaluate generalization capability, all methods, including state-of-the-art approaches [3], [14], [72], [78], [85] and our BUFFER-X, are trained on a single dataset, such as 3DMatch [2] or KITTI [4]. Using the same hyperparameters as BUFFER [14], we conducted a two-stage

TABLE I: Parameters of each module in our BUFFER-X. Note that with this parameter setup, our approach operates in our generalizability benchmark in an out-of-the-box manner without any human intervention.

Param.	Description	Value
κ_{spheric}	Coefficient for voxel size when sphericity is high	0.10
κ_{disc}	Coefficient for voxel size when sphericity is low	0.15
τ_v	Threshold in Eq. (3)	0.05
τ_l	Threshold for the local (l) search radius	0.005
τ_m	Threshold for the middle (m) search radius	0.02
τ_g	Threshold for the global (g) search radius	0.05
δ_v	Sampling ratio for sphericity-based voxelization	10%
N_r	Number of sampling points for radius estimation	2,000
r_{max}	Maximum radius	5.0 m
N_{FPS}	Number of sampled points by FPS	1,500
N_{patch}	Maximum number of points in each patch	512
δ	Truncation threshold for Huber loss	1.0
H	Height of the cylindrical map in Mini-SpinNet	7
W	Sector size of the cylindrical map in Mini-SpinNet	20
D	Feature dimension of the cylindrical map in Mini-SpinNet	32

optimization (*i.e.*, Mini-SpinNet is first trained, followed by training the 3DCCN) and we used Adam optimizer [101] with a learning rate of 0.001, a weight decay of 1e-6, and a learning rate decay of 0.5. We used NVIDIA GeForce RTX 3090 with AMD EPYC 7763 64-Core.

Testing settings. For existing datasets [2]–[4], [8], [10], we follow the conventional given pairs and experimental protocols. The parameters of our approach are summarized in Table I.

Evaluation Metrics. As a key metric, we use the success rate, which directly assesses the robustness of global registration [31]. Specifically, a registration is deemed successful if the translation and rotation errors are within τ_{trans} and τ_{rot} , respectively [41]. For successful cases, we evaluated the performance using relative translation error (RTE) and relative rotation error (RRE), which are defined as follows:

- $\text{RTE} = \sum_{n=1}^{N_{\text{success}}} (\mathbf{t}_{n,\text{GT}} - \hat{\mathbf{t}}_n)^2 / N_{\text{success}}$,
- $\text{RRE} = \frac{180}{\pi} \sum_{n=1}^{N_{\text{success}}} |\cos^{-1}(\frac{\text{Tr}(\hat{\mathbf{R}}_n^T \mathbf{R}_{n,\text{GT}}) - 1}{2})| / N_{\text{success}}$

where $\mathbf{t}_{n,\text{GT}}$ and $\mathbf{R}_{n,\text{GT}}$ denote the n -th ground truth translation and rotation, respectively; N_{success} represents the number of successful registration.

VII. EXPERIMENTAL RESULTS AND DISCUSSION

A. Why existing methods fail to generalize?

First, we demonstrate that existing methods struggle in achieving out-of-the-box generalization, leading to performance degradation due to the issues explained in Sec. III. In this experiment, we mainly used renowned learning-based approaches: FCGF [72], Predator [3], GeoTransformer (*GeoT* for brevity) [78], BUFFER [14], and PARENNet [85].

As shown in Table II, models trained with hyperparameters optimized for one dataset scale (*e.g.*, voxel size and search radius) exhibited substantial performance degradation when applied to datasets with different scales. More critically, as explained in Sec. III-B1, we observed two types of failures when applying methods with mismatched hyperparameters. First, when using indoor parameters (small voxel sizes) on outdoor

TABLE II: Quantitative performance comparison on rate to evaluate generalization capability. Deep learning-based models were trained only on 3DMatch [2] and KITTI [4], respectively, and to ensure a fair comparison, RANSAC was employed for pose estimation across all learning-based approaches, with a maximum of 50K iterations. For conventional methods, FPFH [102] was used for feature extraction.

Env.	Object	Indoor										Outdoor				
		ModelNet40	3DMatch	3DLoMatch	ScanNet++i	ScanNet++F	TIERS	KITTI	WOD	KAIST	MIT	ETH	Oxford			
Conventional	FGR [29] +	84.04	62.53	15.42	77.68	92.31	80.60	98.74	100.00	89.80	74.78	91.87	99.00			
	Quattro [32] +	5.45	8.22	1.74	9.88	97.27	86.57	99.10	100.00	91.46	79.57	51.05	91.03			
	TEASER++ [30] +	86.10	52.00	13.25	66.15	97.22	73.13	98.92	100.00	89.20	71.30	93.69	99.34			
Trained solely on 3DMatch (acquired with a RGB-D sensor)	FCGF [72]	7.35	88.18	40.09	72.90	88.69	55.96	0.00	0.00	0.00	0.00	54.98	0.00			
	+	16.51	88.18	40.09	85.87	88.69	78.62	90.27	97.69	92.91	92.61	54.98	93.68			
	+ +	16.51	88.18	40.09	85.87	88.69	80.11	94.41	97.69	93.55	93.04	55.53	95.68			
	Predator [3]	N/A	90.60	62.40	75.94	OOM	OOM	OOM	OOM	OOM	OOM	OOM	OOM			
	+	84.28	90.60	62.40	75.94	29.81	56.44	0.00	0.00	0.95	0.00	0.14	0.33			
	+ +	84.28	90.60	62.40	75.94	86.01	75.74	77.29	86.92	87.09	79.56	54.42	93.68			
	GeoTransformer [78]	84.36	92.00	75.00	91.18	OOM	OOM	OOM	OOM	OOM	OOM	OOM	OOM			
	+	86.26	92.00	75.00	91.18	7.54	5.06	0.36	0.77	0.25	0.87	0.00	0.33			
	+ +	86.26	92.00	75.00	92.72	97.02	92.99	92.43	89.23	91.86	95.65	71.53	97.01			
	BUFFER [14]	82.39	92.90	71.80	92.72	93.75	62.30	0.00	1.54	0.50	6.96	97.62	0.66			
	+	92.42	92.90	71.80	93.01	94.69	88.96	99.46	100.00	97.24	95.65	99.30	99.00			
	+ +	92.42	92.90	71.80	93.01	94.69	88.96	99.46	100.00	97.24	95.65	99.30	99.00			
	PARENNet [85]	N/A	95.00	80.50	90.84	OOM	OOM	OOM	OOM	OOM	OOM	OOM	OOM			
	+	60.43	95.00	80.50	90.84	43.75	6.21	0.18	0.77	0.75	1.30	1.40	1.66			
	+ +	66.14	95.00	80.50	90.84	87.95	75.06	84.86	92.31	86.44	84.78	69.42	93.36			
Our BUFFER-X with only r_m	99.84	93.38	71.69	93.10	99.60	90.80	99.82	100.00	99.05	95.65	99.30	99.34				
Our BUFFER-X	99.84	95.58	74.18	94.99	99.90	93.45	99.82	100.00	99.15	97.39	99.72	99.67				
Trained solely on KITTI (acquired with a Velodyne HDL-64E LiDAR)	FCGF [72]	7.50	8.04	0.17	19.96	23.07	77.82	98.92	95.38	88.34	82.17	6.59	75.08			
	+	15.32	34.97	4.12	31.00	25.10	77.93	98.92	96.92	94.22	89.13	39.97	86.05			
	+ +	19.19	34.97	4.12	33.37	25.10	77.93	98.92	99.23	94.22	90.43	39.97	90.03			
	Predator [3]	N/A	N/A	N/A	N/A	69.43	99.82	100.00	OOM	54.78	55.68	89.04				
	+	8.60	16.47	0.00	9.40	3.72	69.77	99.82	100.00	71.3	76.52	56.67	89.04			
	+ +	8.60	23.2	3.31	9.40	3.72	69.77	99.82	100.00	94.02	86.08	71.95	95.02			
	GeoTransformer [78]	N/A	N/A	63.84	93.91	77.00	73.42									
	+	74.25	5.94	0.30	15.91	34.18	20.57	99.82	100.00	63.84	93.91	77.56	73.42			
	+ +	74.25	62.17	14.38	76.52	90.63	87.36	99.82	100.00	96.84	96.52	81.77	98.01			
	BUFFER [14]	N/A	N/A	N/A	17.60	88.84	93.34	99.64	100.00	99.50	95.22	98.18	99.34			
	+	95.41	91.19	64.51	93.15	97.81	93.57	99.64	100.00	99.55	97.39	99.86	99.34			
	+ +	95.41	91.19	64.51	93.15	97.81	93.57	99.64	100.00	99.55	97.39	99.86	99.34			
	PARENNet [85]	N/A	N/A	N/A	N/A	N/A	N/A	99.82	97.69	57.51	75.22	68.30	66.11			
	+	34.91	0.77	0.10	3.04	12.00	19.20	99.82	98.46	57.51	75.22	68.44	66.11			
	+ +	83.18	22.09	4.98	29.99	42.91	52.99	99.82	89.50	87.39	72.65	94.02				
Our BUFFER-X with only r_m	99.84	91.96	63.59	92.38	99.45	94.37	99.82	100.00	99.55	99.13	100.00	99.67				
Our BUFFER-X	99.84	93.79	65.89	95.13	99.65	94.83	99.82	100.00	99.55	99.13	100.00	99.67				

: Oracle tuning with manually optimized voxel size and search radius for each dataset.

: Scale down and up alignment, respectively, to normalize dataset scales (e.g., the scale of KITTI, which typically uses a voxel size of 0.3 m, is adjusted to match the scale of 3DMatch, where 0.025 m is commonly used, by dividing by $\frac{0.3}{0.025}$).

N/A: Failure due to too few points remaining after voxelization with the voxel size typically used for larger scale scenes.

OOM: Out-of-memory error caused by excessive memory usage.

datasets, some methods encountered out-of-memory (OOM) errors due to the excessively large number of input points remaining after voxelization. Conversely, when applying outdoor parameters (large voxel sizes) to ModelNet40 and indoor datasets, methods failed due to too few points remaining after voxelization (marked as N/A in Table II).

Once a properly user-tuned voxel size and search radius were provided (referred to as *oracle tuning*, , BUFFER showed remarkable performance improvement owing to its patch-wise input scale normalization characteristics. In contrast, other approaches still showed relatively lower success rates because the networks received point clouds with magnitudes not encountered during training. This potential limitation is further evidenced by the performance improvement of Predator and GeoT after scale alignment (denoted by and), supporting our claim that scale normalization is a key factor in achieving generalizability.

B. Out-of-the-box zero-shot registration performance

Leveraging these insights, our method demonstrates strong zero-shot generalization across diverse datasets without requiring manual hyperparameter tuning. As presented in Table II and Fig. 7, unlike other approaches, our approach demonstrates strong generalization across diverse domains (e.g., object-scale, indoor, and outdoor environments) without requiring oracle tuning or scale alignment. Moreover, even in terms of RTE and RRE, our approach achieves lower errors compared to state-of-the-art methods that use oracle tuning and scale alignment (Fig. 8). These results validate that our algorithm generalizes well across domains while preserving accuracy on in-domain scenarios.

To further evaluate the generalization capability of our approach, we analyze the performance across heterogeneous LiDAR sensor configurations with point clouds captured by different sensors within the same environment. This is a more challenging scenario that requires robustness to varying

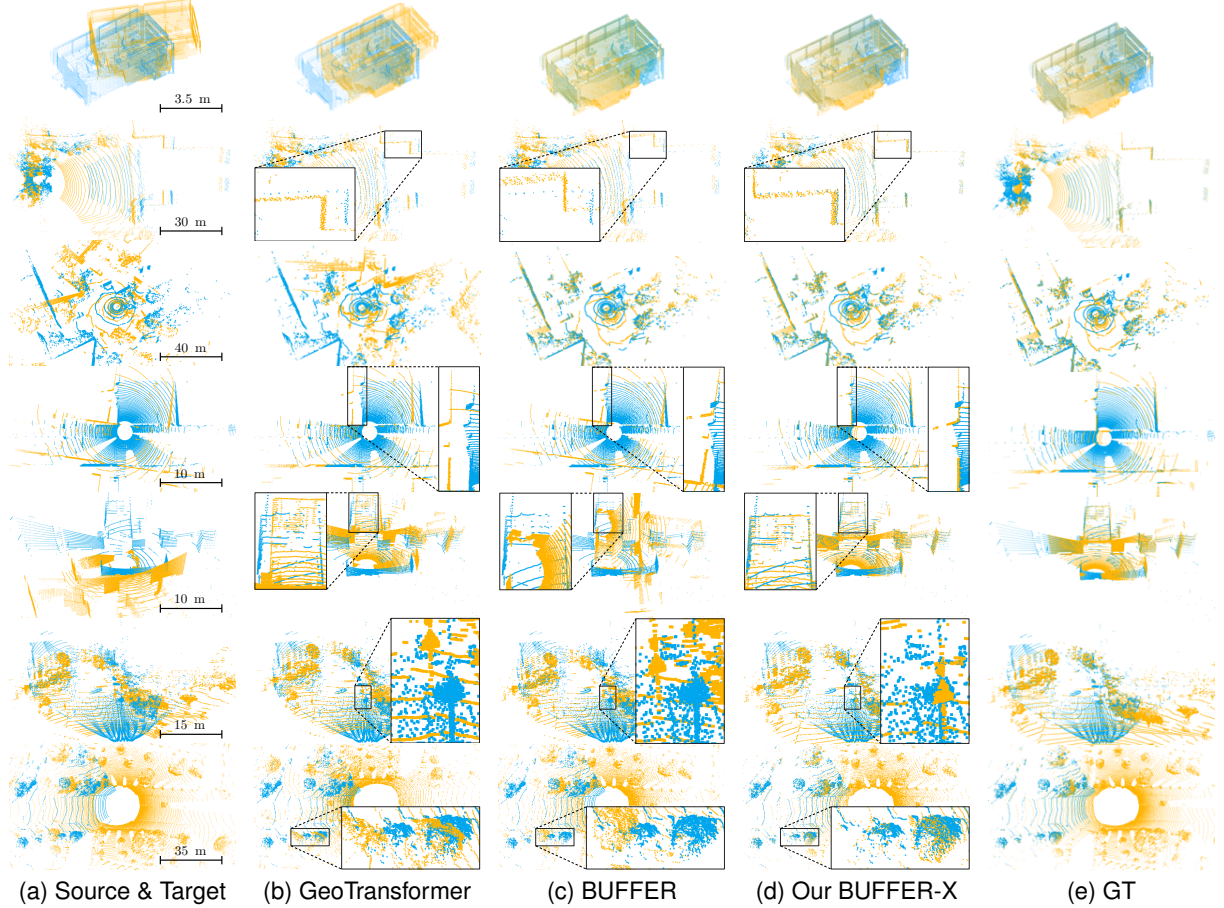


Fig. 7: Qualitative comparison of registration results across diverse scenes (source: orange and target: cyan). All methods were trained on 3DMatch. Top three rows: scan pairs from ScanNet++F, Oxford, and MIT. Bottom four rows: scan pairs with heterogeneous LiDAR sensor setups from Tiers (Vel16→OS128, OS64→Vel16) and KAIST (Aeva→Avia, Ouster→Aeva), respectively, where A→B means that the source acquired by sensor type A is registered to the target point cloud from sensor type B.

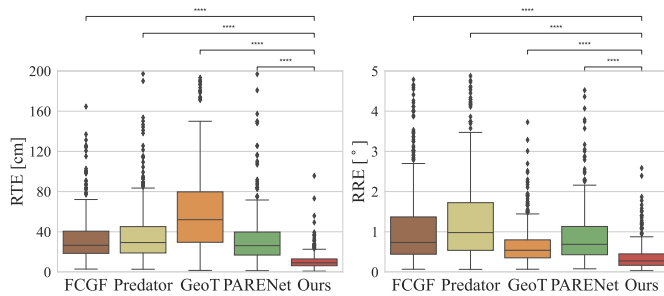


Fig. 8: Relative translation error (RTE) and relative rotation error (RRE) of our approach to state-of-the-art methods, all trained on 3DMatch and tested on KITTI, with oracle tuning and scale alignment, corresponding to those in Table II under the + + setting. The *** annotations indicate measurements with a p -value $< 10^{-4}$ after a paired t -test. Note that even if other state-of-the-art approaches showed promising high success rates in Table II, but in terms of RTE and RRE, our BUFFER-X showed substantially lower values.

sensor characteristics such as different scanning patterns, point

densities, and field of view; see Figs. 5(f), 5(g), and 6(c).

As shown in Table III and the bottom four rows of Fig. 7, our approach demonstrates strong sensor-agnostic generalization capability. First, most existing deep learning methods completely fail without oracle tuning (N/A or 0.00%). Even with oracle tuning and scale alignment, state-of-the-art methods show limited performance, highlighting severe brittleness to sensor variations. In contrast, our approach achieves the highest success rates across all six sensor pairs without any manual tuning, even for challenging cases such as very sparse point clouds to dense clouds (*i.e.*, Vel16 → OS128), showing lower performance degradation compared to other approaches. Furthermore, we analyzed the rationale at the patch-level. As illustrated in Fig. 9, although density distributions and fields of view differ across sensors, the patch-level features extracted by our method remain consistent.

Therefore, this experimental evidence validates that our geometric bootstrapping, patch-wise normalization, and multi-scale matching strategy effectively handles the variations in point cloud characteristics introduced by different sensor types, making our method sensor-agnostic.

TABLE III: Registration success rates under heterogeneous sensor configurations. Deep learning-based methods are trained only on 3DMatch [2]. Conventional methods use FPFH [102]. To ensure a fair comparison, RANSAC was employed for pose estimation across all learning-based approaches, with a maximum of 50K iterations.

	Dataset	TIERS			KAIST			Average rank
		OS128 → OS64	OS64 → Vel16	Vel16 → OS128	Aeva → Avia	Avia → Ouster	Ouster → Aeva	
Conventional	FGR [29] +	61.57	71.49	32.57	39.27	48.79	72.10	7.67
	Quatros [32] +	75.78	90.06	48.08	51.67	51.90	76.51	5.67
	TEASER++ [30] +	62.11	64.76	27.96	28.93	38.28	63.29	8.50
Deep learning-based (Trained solely on 3DMatch)	FCGF [72]	0.00	0.00	0.00	0.00	0.00	0.00	13.83
	+	28.95	30.05	29.03	27.34	22.58	12.04	9.50
	+ +	28.95	30.05	29.03	27.34	22.58	12.04	9.50
	Predator [3]	N/A	N/A	N/A	N/A	N/A	N/A	13.50
	+	1.62	0.00	0.00	0.00	0.00	0.00	13.17
	+ +	25.03	18.38	10.71	20.19	14.48	21.59	10.83
	GeoTransformer [78]	N/A	N/A	N/A	N/A	N/A	N/A	13.17
	+	0.27	0.22	0.05	0.00	0.00	0.00	12.67
	+ +	85.25	83.24	55.90	76.79	73.79	56.97	5.67
	BUFFER [14]	7.98	3.89	2.48	0.00	0.00	0.15	11.83
	+	92.83	88.54	66.77	91.57	90.52	97.06	3.17
	+ +	92.83	88.54	66.77	91.57	90.52	97.06	3.17
	PARENNet [85]	N/A	N/A	N/A	N/A	N/A	N/A	12.33
	+	0.00	0.00	0.00	0.00	0.00	0.00	12.33
	+ +	65.90	59.78	37.42	75.84	70.52	53.60	6.67
Our BUFFER-X with only r_m		95.40	96.86	77.33	96.04	93.80	97.20	2.00
Our BUFFER-X		98.92	99.46	84.32	97.62	96.03	98.24	1.00

Oracle tuning with manually optimized voxel size and search radius for each dataset.

Scale down alignment to normalize dataset scales.

N/A: Failure due to too few points remaining after voxelization with the voxel size typically used for larger scale scenes.

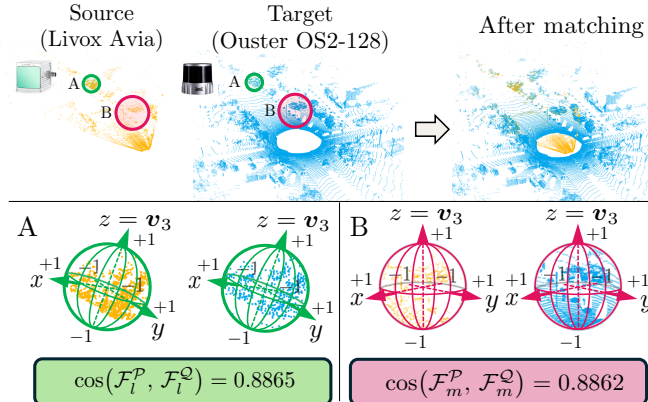


Fig. 9: Visualization of patch-level similarity across heterogeneous LiDAR sensors. Despite large differences in overall point density distributions and fields of view captured by Livox Avia and Ouster OS2-128, local patches from different point clouds (A and B) exhibit consistent feature distributions, showing high cosine similarity close to 1.

C. In-depth analysis of key components

Point normalization for domain-invariant features. To understand why our approach achieves superior generalization, we first analyze the feature distributions using PaCMAP visualization [103], which preserves relative distances between data points better than t-SNE [104]. As presented in Fig. 10, unlike state-of-the-art approaches that exhibit domain-specific clustering, our approach demonstrates persistent descriptor distributions across domain shift, as evidenced by the significant overlap between 3DMatch (training domain) and other unseen datasets. This validates that our point normalization strategy effectively produces domain-invariant features, which is a key

TABLE IV: Ablation study on multi-scale combinations and early exit strategies evaluated on 3DMatch [2]. Top: different scale combinations. Bottom: comparison with RANSAC and KISS-Matcher solver [84] (referred to as *our solver*) for early exit.

Local	Middle	Global	RTE [cm] ↓	RRE [°] ↓	Succ. rate [%] ↑	Hz ↑	
✓	✓	✓	6.57	2.15	84.06	5.61	
			5.87	1.85	93.38	5.47	
	✓		6.06	1.91	93.57	5.49	
			5.73	1.81	94.31	2.35	
✓	✓	✓	5.77	1.81	94.02	2.36	
✓	✓	✓	5.78	1.81	94.62	2.33	
✓	✓	✓	5.78	1.79	95.58	1.81	
W/ Early Exit			RTE [cm] ↓	RRE [°] ↓	Succ. rate [%] ↑	Hz ↑	
W/ RANSAC, $\tau_N = 10$			5.87	1.85	93.38	5.47	
W/ RANSAC, $\tau_N = 50$			5.83	1.79	94.54	5.19	
W/ our solver, $\tau_N = 10$			5.88	1.78	93.94	5.15	
W/ our solver, $\tau_N = 50$			5.79	1.79	94.95	4.72	

factor enabling zero-shot generalization.

Multi-scale matching strategy. To understand the contribution of our multi-scale matching strategy, we analyze how correspondences at different scales complement each other. Fig. 11 shows the distribution of correspondences found at different scales (global, middle, local) across datasets, revealing that each scale captures distinct correspondence patterns. This experimental evidence indicates that certain correspondences can only be obtained when considering multiple scales, as those found at a local scale are not necessarily a subset of those at a global scale.

Table IV quantifies this observation. While using only the middle scale achieves 93.38% success rate at 5.47 Hz, incorporating all three scales increases the success rate to 95.58%, confirming that correspondences across scales com-

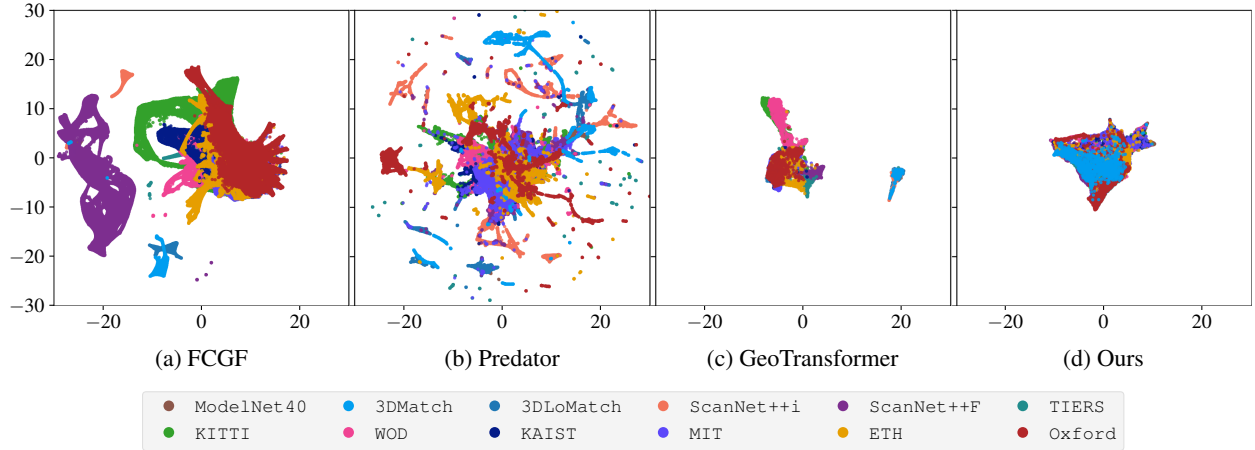


Fig. 10: PaCMAP visualization of descriptor distributions across datasets. Unlike state-of-the-art approaches [3], [72], [78], our BUFFER-X shows persistent descriptors that are robust to domain shift, as evidenced by the overlap between 3DMatch (training domain) and other datasets. That is, the closer and more overlapped with sky blue, the better.

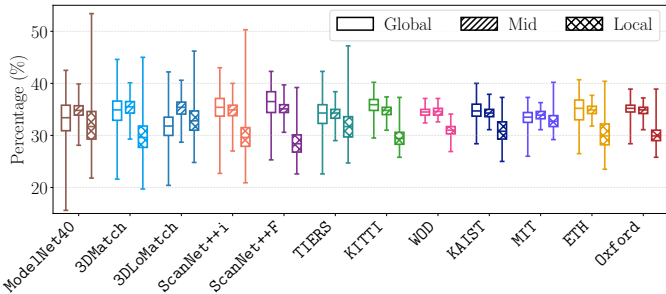


Fig. 11: Distribution of correspondences at different scales (global, middle, local) across datasets, showing the contribution of multi-scale matching.

plement each other. However, this improvement comes at the cost of reduced speed (1.81 Hz), introducing a trade-off between accuracy and computational efficiency. This allows users to balance performance and speed based on their specific application requirements.

D. Analysis of BUFFER-X-Lite

Next, we examine how computational efficiency can be improved by combining early exit strategy with KISS-Matcher solver [84], as explained in Sec. V. As shown in Fig. 12, with $\tau_N = 25$ as an example, the early exit variant takes only 56.8% of the time required by the full multi-scale approach on average across all datasets while maintaining comparable accuracy. Fig. 13 shows that KISS-Matcher solver takes less time than RANSAC, making it particularly suitable for our early exit strategy, which requires multiple pose estimations.

Furthermore, KISS-Matcher solver is particularly well-suited for early exit strategy because it can easily detect failure cases by checking the cardinality of final inliers. As presented in Fig. 14, given the same number of initial correspondences, KISS-Matcher solver separates success and failure cases more clearly using only the number of final inliers. This enables easier failure detection; as shown in Table IV, with the same

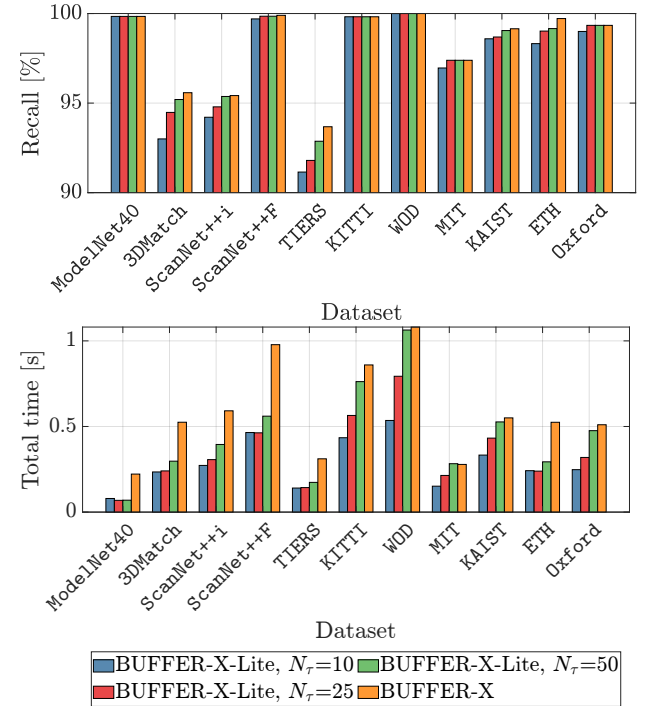


Fig. 12: Comparison of success rate and total computation time between BUFFER-X-Lite, which is the efficient version of BUFFER-X, and the original BUFFER-X.

threshold, the early exit variant with KISS-Matcher solver achieves higher success rates. This is because with RANSAC, the number of inliers in failure cases is relatively widespread across lower values, whereas KISS-Matcher solver failures typically have final inlier counts close to zero.

This analysis demonstrates that the early exit strategy provides a practical way to balance accuracy and computational efficiency depending on application requirements.

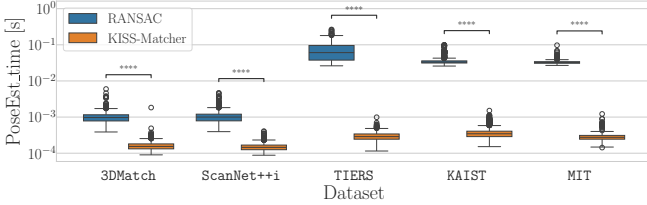


Fig. 13: Pose estimation time comparison between RANSAC and KISS-Matcher solver given the same correspondences. RANSAC, which is still widely used for pose estimation in learning-based approaches, exhibits substantially longer computation time for LiDAR-acquired point clouds (*i.e.*, in TIERS, KAIST, and MIT), whereas KISS-Matcher solver achieves up to 100 \times faster performance.

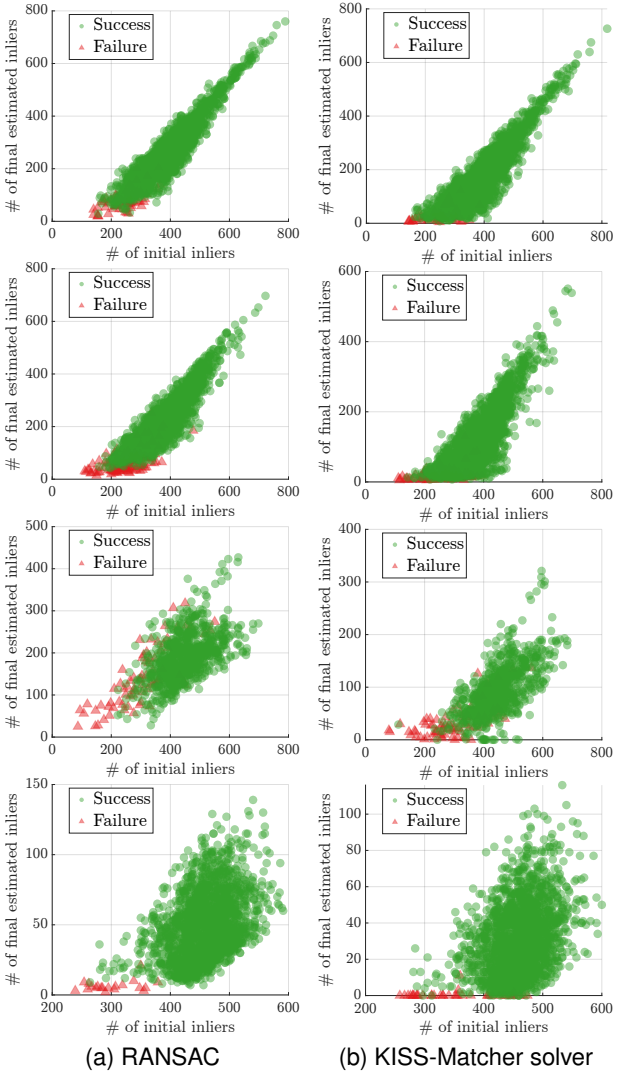


Fig. 14: Comparison of mutual correspondences versus inliers for RANSAC and KISS-Matcher solver across 3DMatch, ScanNet++i, TIERS, and KAIST. The number of estimated inliers in failure cases for RANSAC is relatively widespread across lower values, whereas that of KISS-Matcher solver is more likely to be near-zero.

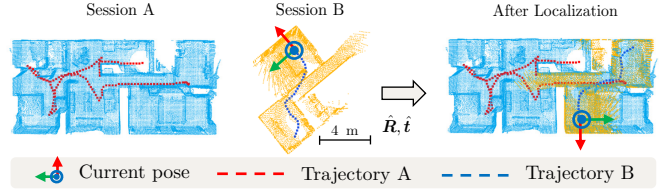


Fig. 15: Application of our approach to robotic systems: online submap-to-map localization between two sessions on the Cantwell scene from the Gibson dataset [106].

E. Application: Submap-to-map localization

As an application, BUFFER-X can be exploited for robotic localization in long-term, multi-session environments. In such settings, a key challenge is localizing within a pre-built map without relying on pose initialization or GPS, especially when the robot resumes operation after significant time gaps [105]. This scenario, commonly referred to as the *kidnapped robot* problem, arises in practical deployments such as daily autonomous delivery or multi-day inspection missions.

As shown in Fig. 15, our proposed approach enables robust submap-to-map localization without pose priors. During online operation, the robot incrementally constructs a local submap from recent LiDAR scans. When localization is required, our approach registers this submap against a pre-built global map using zero-shot registration, directly estimating the robot’s global pose without manual tuning. Importantly, our proposed method does not need re-training, enabling easy deployment without environment-specific training or tuning. This suggests that the approach has the potential to support multi-session localization in both indoor and outdoor environments.

F. Limitations

As seen in Table II, our approach showed lower success rate in 3DLoMatch, which has only 10–30% overlap. This is because Eq. (9) selects correspondences with the largest cardinality as inliers. However, in partial overlap scenarios, maximizing the number of correspondences might not yield the actual global optimum (*i.e.*, there might exist \mathcal{I}^* that satisfies $|\mathcal{I}^*| \leq |\mathcal{I}|$ but leads to a better relative pose estimate). This highlights a trade-off between generalization and robustness to partial overlaps.

VIII. CONCLUSION

This paper addresses zero-shot generalization in point cloud registration by identifying three fundamental limitations: fixed user-defined parameters, learned keypoint detectors with poor transferability, and absolute coordinates that amplify scale mismatches. To overcome these barriers, we presented *BUFFER-X*, a training-free framework achieving zero-shot generalization through geometric bootstrapping, distribution-aware sampling, and hierarchical multi-scale matching with patch-based normalization. For efficiency, we introduced *BUFFER-X-Lite*, which achieves a substantial reduction in computation time through adaptive early exit and KISS-Matcher solver, enabling practical trade-offs between speed and accuracy.

We evaluated on a comprehensive benchmark spanning 12 datasets across environmental scales, scanning patterns, acquisition setups, and geographic regions, including heterogeneous LiDAR configurations. Results demonstrate effective generalization without manual tuning, with *BUFFER-X-Lite* providing practical trade-offs between speed and accuracy for real-world deployment. Future work will explore integrating semantic cues to improve robustness in extremely low-overlap scenarios while maintaining zero-shot generalization capability.

REFERENCES

- [1] Z. Wu, S. Song, A. Khosla, F. Yu, L. Zhang, X. Tang, and J. Xiao, “3D shapenets: A deep representation for volumetric shapes,” in *IEEE Conf. on Computer Vision and Pattern Recognition (CVPR)*, 2015, pp. 1912–1920. [1](#), [2](#), [7](#)
- [2] A. Zeng, S. Song, M. Nießner, M. Fisher, J. Xiao, and T. Funkhouser, “3DMatch: Learning the matching of local 3d geometry in range scans,” in *IEEE Conf. on Computer Vision and Pattern Recognition (CVPR)*, 2017, p. 4. [1](#), [2](#), [3](#), [7](#), [9](#), [10](#), [12](#)
- [3] S. Huang, Z. Gojcic, M. Usvyatsov, A. Wieser, and K. Schindler, “PREDATOR: Registration of 3D Point Clouds with Low Overlap,” in *IEEE Conf. on Computer Vision and Pattern Recognition (CVPR)*, Jun. 2021, pp. 4265–4274. [1](#), [2](#), [3](#), [7](#), [9](#), [10](#), [12](#), [13](#)
- [4] A. Geiger, P. Lenz, C. Stiller, and R. Urtasun, “Vision meets robotics: The KITTI dataset,” *Intl. J. of Robotics Research*, vol. 32, no. 11, pp. 1231–1237, 2013. [1](#), [2](#), [3](#), [7](#), [9](#), [10](#)
- [5] C. Yeshwanth, Y.-C. Liu, M. Nießner, and A. Dai, “Scannet++: A high-fidelity dataset of 3d indoor scenes,” in *Proceedings of the IEEE/CVF International Conference on Computer Vision*, 2023, pp. 12–22. [1](#), [7](#)
- [6] L. Qingqing, Y. Xianjia, J. P. Queralta, and T. Westerlund, “Multi-modal LiDAR dataset for benchmarking general-purpose localization and mapping algorithms,” in *IEEE/RSJ Intl. Conf. on Intelligent Robots and Systems (IROS)*, 2022, pp. 3837–3844. [1](#), [2](#), [3](#), [7](#), [8](#)
- [7] M. Ramezani, Y. Wang, M. Camurri, D. Wisth, M. Mattamala, and M. Fallon, “The newer college dataset: Handheld lidar, inertial and vision with ground truth,” in *2020 IEEE/RSJ International Conference on Intelligent Robots and Systems (IROS)*. IEEE, 2020, pp. 4353–4360. [1](#), [7](#), [8](#), [9](#)
- [8] P. Sun, H. Kretschmar, X. Dotiwalla, A. Chouard, V. Patnaik, P. Tsui, J. Guo, Y. Zhou, Y. Chai, B. Caine *et al.*, “Scalability in perception for autonomous driving: Waymo open dataset,” in *Proceedings of the IEEE/CVF Conference on Computer Vision and Pattern Recognition*, 2020, pp. 2446–2454. [1](#), [7](#), [9](#)
- [9] Y. Tian, Y. Chang, L. Quang, A. Schang, C. Nieto-Granda, J. How, and L. Carlone, “Resilient and distributed multi-robot visual SLAM: Datasets, experiments, and lessons learned,” in *IEEE/RSJ Intl. Conf. on Intelligent Robots and Systems (IROS)*, 2023. [1](#), [7](#), [8](#)
- [10] F. Pomerleau, M. Liu, F. Colas, and R. Siegwart, “Challenging data sets for point cloud registration algorithms,” *The International Journal of Robotics Research*, vol. 31, no. 14, pp. 1705–1711, 2012. [1](#), [7](#), [9](#)
- [11] M. Jung, W. Yang, D. Lee, H. Gil, G. Kim, and A. Kim, “HeLiPR: Heterogeneous LiDAR dataset for inter-LiDAR place recognition under spatial and temporal variations,” *The International Journal of Robotics Research*, 2023. [1](#), [2](#), [7](#), [8](#), [9](#)
- [12] S. Ao, Y. Guo, S. Gu, J. Tian, and D. Li, “SGHs for 3D local surface description,” *IET Computer Vision*, vol. 14, no. 4, pp. 154–161, 2020. [1](#)
- [13] S. Ao, Y. Guo, J. Tian, Y. Tian, and D. Li, “A repeatable and robust local reference frame for 3D surface matching,” *Pattern Recognition*, vol. 100, p. 107186, 2020. [1](#)
- [14] S. Ao, Q. Hu, H. Wang, K. Xu, and Y. Guo, “BUFFER: Balancing accuracy, efficiency, and generalizability in point cloud registration,” in *IEEE Conf. on Computer Vision and Pattern Recognition (CVPR)*, 2023, pp. 1255–1264. [1](#), [2](#), [3](#), [4](#), [5](#), [7](#), [9](#), [10](#), [12](#)
- [15] S. Ao, Q. Hu, B. Yang, A. Markham, and Y. Guo, “SpinNet: Learning a general surface descriptor for 3D point cloud registration,” in *IEEE Conf. on Computer Vision and Pattern Recognition (CVPR)*, 2021, pp. 11 753–11 762. [1](#), [2](#), [3](#), [4](#), [5](#)
- [16] H. Chen, P. Yan, S. Xiang, and Y. Tan, “Dynamic cues-assisted transformer for robust point cloud registration,” in *Proceedings of the IEEE/CVF Conference on Computer Vision and Pattern Recognition*, 2024, pp. 21 698–21 707. [1](#), [2](#)
- [17] J. Mu, L. Bie, S. Du, and Y. Gao, “ColorPCR: Color point cloud registration with multi-stage geometric-color fusion,” in *Proceedings of the IEEE/CVF Conference on Computer Vision and Pattern Recognition*, 2024, pp. 21 061–21 070. [1](#)
- [18] G. Chen, M. Wang, Y. Yang, L. Yuan, and Y. Yue, “Fast and robust point cloud registration with tree-based transformer,” in *2024 IEEE International Conference on Robotics and Automation (ICRA)*, 2024, pp. 773–780. [1](#)
- [19] Y. Zhang, H. Zhao, H. Li, and S. Chen, “FastMAC: Stochastic Spectral Sampling of Correspondence Graph,” in *Proceedings of the IEEE/CVF Conference on Computer Vision and Pattern Recognition*, 2024, pp. 17 857–17 867. [1](#)
- [20] X. Zhang, J. Yang, S. Zhang, and Y. Zhang, “3D registration with maximal cliques,” in *Proceedings of the IEEE/CVF Conference on Computer Vision and Pattern Recognition*, 2023, pp. 17 745–17 754. [1](#)
- [21] K. Fathian and T. Summers, “CLIPPER+: A Fast Maximal Clique Algorithm for Robust Global Registration,” *IEEE Robotics and Automation Letters*, 2024. [1](#)
- [22] S. Liu, T. Wang, Y. Zhang, R. Zhou, L. Li, C. Dai, Y. Zhang, L. Wang, and H. Wang, “Deep semantic graph matching for large-scale outdoor point cloud registration,” *IEEE Transactions on Geoscience and Remote Sensing*, 2024. [1](#)
- [23] X. Liu, R. Qin, J. Yan, and J. Yang, “Ncmnet: Neighbor consistency mining network for two-view correspondence pruning,” *IEEE Transactions on Pattern Analysis and Machine Intelligence*, 2024. [1](#)
- [24] Y. Yuan, Y. Wu, X. Fan, M. Gong, Q. Miao, and W. Ma, “Inlier confidence calibration for point cloud registration,” in *Proceedings of the IEEE/CVF Conference on Computer Vision and Pattern Recognition*, 2024, pp. 5312–5321. [1](#), [2](#)
- [25] Q. Liu, H. Zhu, Z. Wang, Y. Zhou, S. Chang, and M. Guo, “Extend your own correspondences: Unsupervised distant point cloud registration by progressive distance extension,” in *Proceedings of the IEEE/CVF Conference on Computer Vision and Pattern Recognition*, 2024, pp. 20 816–20 826. [1](#), [2](#), [9](#)
- [26] P. Shi, S. Yan, Y. Xiao, X. Liu, Y. Zhang, and J. Li, “RANSAC back to SOTA: A two-stage consensus filtering for real-time 3D registration,” *IEEE Robotics and Automation Letters*, 2024. [1](#), [3](#)
- [27] T. Huang, L. Peng, R. Vidal, and Y.-H. Liu, “Scalable 3D Registration via Truncated Entry-wise Absolute Residuals,” in *Proceedings of the IEEE/CVF Conference on Computer Vision and Pattern Recognition (CVPR)*, June 2024, pp. 27 477–27 487. [1](#)
- [28] J. Yang, X. Zhang, P. Wang, Y. Guo, K. Sun, Q. Wu, S. Zhang, and Y. Zhang, “MAC: Maximal Cliques for 3D Registration,” *IEEE Transactions on Pattern Analysis and Machine Intelligence*, 2024. [1](#)
- [29] Q.-Y. Zhou, J. Park, and V. Koltun, “Fast global registration,” in *Proceedings of the European Conference on Computer Vision (ECCV)*, 2016, pp. 766–782. [1](#), [2](#), [10](#), [12](#)
- [30] H. Yang, J. Shi, and L. Carlone, “TEASER: Fast and Certifiable Point Cloud Registration,” *IEEE Trans. Robotics*, vol. 37, no. 2, pp. 314–333, 2020. [1](#), [2](#), [6](#), [10](#), [12](#)
- [31] H. Lim, B. Kim, D. Kim, E. Mason Lee, and H. Myung, “Quattro++: Robust global registration exploiting ground segmentation for loop closing in LiDAR SLAM,” *Intl. J. of Robotics Research*, pp. 685–715, 2024. [1](#), [2](#), [9](#)
- [32] H. Lim, S. Yeon, S. Ryu, Y. Lee, Y. Kim, J. Yun, E. Jung, D. Lee, and H. Myung, “A single correspondence is enough: Robust global registration to avoid degeneracy in urban environments,” in *IEEE Intl. Conf. on Robotics and Automation (ICRA)*, 2022, pp. 8010–8017. [1](#), [2](#), [10](#), [12](#)
- [33] J. Yang, H. Li, D. Campbell, and Y. Jia, “Go-ICP: A globally optimal solution to 3D ICP point-set registration,” *IEEE Trans. Pattern Anal. Machine Intell.*, vol. 38, no. 11, pp. 2241–2254, Nov. 2016. [1](#), [2](#)
- [34] L. Bernreiter, L. Ott, J. Nieto, R. Siegwart, and C. Cadena, “PHASER: A robust and correspondence-free global point cloud registration,” *IEEE Robotics and Automation Letters*, vol. 6, no. 2, pp. 855–862, 2021. [1](#), [2](#)
- [35] P. Yin, S. Yuan, H. Cao, X. Ji, S. Zhang, and L. Xie, “Segregator: Global point cloud registration with semantic and geometric cues,” in *IEEE Intl. Conf. on Robotics and Automation (ICRA)*, 2023, pp. 2848–2854. [1](#)
- [36] F. Poiesi and D. Boscaini, “Learning general and distinctive 3D local deep descriptors for point cloud registration,” *IEEE Trans. Pattern Anal. Machine Intell.*, vol. 45, no. 3, pp. 3979–3985, 2022. [1](#)
- [37] A. Dosovitskiy and J. Djolonga, “You only train once: Loss-conditional training of deep networks,” in *International conference on learning representations*, 2019. [1](#)

[38] T. Chen, B. Ji, T. Ding, B. Fang, G. Wang, Z. Zhu, L. Liang, Y. Shi, S. Yi, and X. Tu, "Only train once: A one-shot neural network training and pruning framework," *Advances in Neural Information Processing Systems*, vol. 34, pp. 19 637–19 651, 2021. [1](#)

[39] W. Wang, W. Ren, G. Mei, B. Ren, X. Huang, F. Poiesi, N. Sebe, and B. Lepri, "Zeroeg: Zero-shot point cloud registration with foundation models," 2024. [Online]. Available: <https://arxiv.org/abs/2312.03032> [1, 2](#)

[40] C. Zheng, J. Huang, H. Chen, and M. Wei, "Rare: Refine any registration of pairwise point clouds via zero-shot learning," 2025. [Online]. Available: <https://arxiv.org/abs/2507.19950> [1, 2](#)

[41] Z. Yew and G. Lee, "3dfeat-net: Weakly supervised local 3d features for point cloud registration," in *European Conf. on Computer Vision (ECCV)*, 2018. [2, 6, 7, 9](#)

[42] H. Lim, S. Jang, B. Mersch, J. Behley, H. Myung, and C. Stachniss, "Helimos: A dataset for moving object segmentation in 3d point clouds from heterogeneous lidar sensors," in *IEEE/RSJ International Conference on Intelligent Robots and Systems (IROS)*, 2024, pp. 14 087–14 094. [2](#)

[43] M. Seo, H. Lim, K. Lee, L. Carlone, and J. Park, "BUFFER-X: Towards zero-shot point cloud registration in diverse scenes," *arXiv preprint arXiv:2503.07940*, 2025. [2, 3, 5, 9](#)

[44] K. Aoki, K. Koide, S. Oishi, M. Yokozuka, A. Banno, and J. Meguro, "3D-BBS: Global localization for 3D point cloud scan matching using branch-and-bound algorithm," *IEEE Intl. Conf. on Robotics and Automation (ICRA)*, pp. 1796–1802, 2024. [2](#)

[45] H. Yin, X. Xu, S. Lu, X. Chen, R. Xiong, S. Shen, C. Stachniss, and Y. Wang, "A survey on global lidar localization: Challenges, advances and open problems," *Intl. J. of Computer Vision*, pp. 1–33, 2024. [2](#)

[46] X. Chen, T. Läbe, A. Milioto, T. Röhling, J. Behley, and C. Stachniss, "OverlapNet: A siamese network for computing LiDAR scan similarity with applications to loop closing and localization," *Autonomous Robots*, vol. 46, no. 1, pp. 61–81, 2022. [2](#)

[47] D. Cattaneo, M. Vaghi, and A. Valada, "LCDNet: Deep loop closure detection and point cloud registration for LiDAR SLAM," *IEEE Trans. Robotics*, vol. 38, no. 4, pp. 2074–2093, 2022. [2](#)

[48] K. Lee, J. Lee, and J. Park, "Learning to register unbalanced point pairs," *arXiv preprint arXiv:2207.04221*, 2022. [2](#)

[49] P. J. Besl and N. D. McKay, "A method for registration of 3-D shapes," *IEEE Trans. Pattern Anal. Machine Intell.*, vol. 14, no. 2, 1992. [2](#)

[50] A. Segal, D. Haehnel, and S. Thrun, "Generalized ICP," in *Robotics: Science and Systems (RSS)*, Jun. 2009. [2](#)

[51] F. Pomerleau, F. Colas, R. Siegwart, and S. Magnenat, "Comparing ICP variants on real-world data sets," *Autonomous Robots*, vol. 34, no. 3, pp. 133–148, 2013. [2](#)

[52] K. Koide, M. Yokozuka, S. Oishi, and A. Banno, "Voxelized GICP for fast and accurate 3D point cloud registration," in *IEEE Intl. Conf. on Robotics and Automation (ICRA)*, 2021, pp. 11 054–11 059. [2](#)

[53] F. Pomerleau, M. Liu, F. Colas, and R. Siegwart, "Challenging data sets for point cloud registration algorithms," *Intl. J. of Robotics Research*, vol. 31, no. 14, pp. 1705–1711, 2012. [2](#)

[54] I. Vizzo, T. Guadagnino, B. Mersch, L. Wiesmann, J. Behley, and C. Stachniss, "KISS-ICP: In defense of point-to-point ICP – Simple, accurate, and robust registration if done the right way," *IEEE Robotics and Automation Letters*, pp. 1029–1036, 2023. [2](#)

[55] M. Fischler and R. Bolles, "Random sample consensus: a paradigm for model fitting with application to image analysis and automated cartography," *Commun. ACM*, vol. 24, pp. 381–395, 1981. [2, 6](#)

[56] Z. Dong, B. Yang, Y. Liu, F. Liang, B. Li, and Y. Zang, "A novel binary shape context for 3D local surface description," *ISPRS Journal of Photogrammetry and Remote Sensing*, vol. 130, pp. 431–452, 2017. [2](#)

[57] H. Yang and L. Carlone, "A polynomial-time solution for robust registration with extreme outlier rates," in *Robotics: Science and Systems (RSS)*, 2019. [2](#)

[58] M. Rouhani and A. D. Sappa, "Correspondence free registration through a point-to-model distance minimization," in *Intl. Conf. on Computer Vision (ICCV)*, 2011, pp. 2150–2157. [2](#)

[59] M. Brown, D. Windridge, and J.-Y. Guillemaut, "A family of globally optimal branch-and-bound algorithms for 2D-3D correspondence-free registration," *Pattern Recognition*, vol. 93, pp. 36–54, 2019. [2](#)

[60] C. Papazov, S. Haddadin, S. Parusel, K. Krieger, and D. Burschka, "Rigid 3D geometry matching for grasping of known objects in cluttered scenes," *Intl. J. of Robotics Research*, vol. 31, no. 4, pp. 538–553, 2012. [2](#)

[61] O. Chum, J. Matas, and J. Kittler, "Locally optimized RANSAC," in *Joint Pattern Recognition Symposium*, 2003, pp. 236–243. [2](#)

[62] S. Choi, T. Kim, and W. Yu, "Performance evaluation of RANSAC family," *J. of Computer Vision*, vol. 24, no. 3, pp. 271–300, 1997. [2](#)

[63] R. Schnabel, R. Wahl, and R. Klein, "Efficient RANSAC for point-cloud shape detection," in *Computer Graphics Forum*, 2007, pp. 214–226. [2](#)

[64] C. Olsson, F. Kahl, and M. Oskarsson, "Branch-and-bound methods for euclidean registration problems," *IEEE Trans. Pattern Anal. Machine Intell.*, vol. 31, no. 5, pp. 783–794, 2009. [2](#)

[65] R. Hartley and F. Kahl, "Global optimization through rotation space search," *Intl. J. of Computer Vision*, vol. 82, no. 1, pp. 64–79, 2009. [2](#)

[66] J. Pan, Z. Min, A. Zhang, H. Ma, and M. Q.-H. Meng, "Multi-view global 2D-3D registration based on branch and bound algorithm," in *Proc. IEEE Int. Conf. Robot. Biomim.*, 2019, pp. 3082–3087. [2](#)

[67] M. Zhao, J. Jiang, L. Ma, S. Xin, G. Meng, and D.-M. Yan, "Correspondence-free non-rigid point set registration using unsupervised clustering analysis," in *Proceedings of the IEEE/CVF Conference on Computer Vision and Pattern Recognition*, 2024, pp. 21 199–21 208. [2](#)

[68] H. Lei, G. Jiang, and L. Quan, "Fast descriptors and correspondence propagation for robust global point cloud registration," *IEEE Trans. Image Processing*, vol. 26, no. 8, pp. 3614–3623, 2017. [2](#)

[69] Z. Yu, Z. Qin, L. Zheng, and K. Xu, "Learning instance-aware correspondences for robust multi-instance point cloud registration in cluttered scenes," in *Proceedings of the IEEE/CVF Conference on Computer Vision and Pattern Recognition (CVPR)*, June 2024, pp. 19 605–19 614. [2](#)

[70] G. Mei, H. Tang, X. Huang, W. Wang, J. Liu, J. Zhang, L. V. Gool, and Q. Wu, "Unsupervised deep probabilistic approach for partial point cloud registration," 2023. [Online]. Available: <https://arxiv.org/abs/2303.13290> [2](#)

[71] C. R. Qi, H. Su, K. Mo, and L. J. Guibas, "Pointnet: Deep learning on point sets for 3D classification and segmentation," in *IEEE Conf. on Computer Vision and Pattern Recognition (CVPR)*, 2017, pp. 652–660. [2](#)

[72] C. Choy, J. Park, and V. Koltun, "Fully convolutional geometric features," in *Intl. Conf. on Computer Vision (ICCV)*, 2019, pp. 8958–8966. [2, 9, 10, 12, 13](#)

[73] C. Choy, W. Dong, and V. Koltun, "Deep global registration," in *IEEE Conf. on Computer Vision and Pattern Recognition (CVPR)*, 2020. [2](#)

[74] C. Choy, J. Gwak, and S. Savarese, "4D Spatio-Temporal Convnets: Minkowski convolutional neural networks," in *IEEE Conf. on Computer Vision and Pattern Recognition (CVPR)*, 2019, pp. 3075–3084. [2](#)

[75] X. Zhu, H. Zhou, T. Wang, F. Hong, Y. Ma, W. Li, H. Li, and D. Lin, "Cylindrical and asymmetrical 3d convolution networks for lidar segmentation," in *Proceedings of the IEEE/CVF conference on computer vision and pattern recognition*, 2021, pp. 9939–9948. [2](#)

[76] H. Thomas, C. R. Qi, J.-E. Deschaud, B. Marcotegui, F. Goulette, and L. J. Guibas, "Kpconv: Flexible and deformable convolution for point clouds," in *Proceedings of the IEEE/CVF international conference on computer vision*, 2019, pp. 6411–6420. [2](#)

[77] X. Bai, Z. Luo, L. Zhou, H. Fu, L. Quan, and C.-L. Tai, "D3feat: Joint learning of dense detection and description of 3d local features," in *IEEE Conf. on Computer Vision and Pattern Recognition (CVPR)*, 2020. [2](#)

[78] Z. Qin, H. Yu, C. Wang, Y. Guo, Y. Peng, S. Ilic, D. Hu, and K. Xu, "GeoTransformer: Fast and robust point cloud registration with geometric transformer," *IEEE Transactions on Pattern Analysis and Machine Intelligence*, vol. 45, no. 8, pp. 9806–9821, 2023. [2, 3, 9, 10, 12, 13](#)

[79] X. Wu, Y. Lao, L. Jiang, X. Liu, and H. Zhao, "Point transformer v2: Grouped vector attention and partition-based pooling," *Advances in Neural Information Processing Systems*, vol. 35, pp. 33 330–33 342, 2022. [2](#)

[80] X. Wu, L. Jiang, P.-S. Wang, Z. Liu, X. Liu, Y. Qiao, W. Ouyang, T. He, and H. Zhao, "Point Transformer V3: Simpler Faster Stronger," in *Proceedings of the IEEE/CVF Conference on Computer Vision and Pattern Recognition*, 2024, pp. 4840–4851. [2](#)

[81] H. Yu, Z. Qin, J. Hou, M. Saleh, D. Li, B. Busam, and S. Ilic, "Rotation-invariant transformer for point cloud matching," in *CVPR*, 2023. [2](#)

[82] S. Ao, Y. Guo, Q. Hu, B. Yang, A. Markham, and Z. Chen, "You only train once: Learning general and distinctive 3d local descriptors," *IEEE Transactions on Pattern Analysis and Machine Intelligence*, vol. 45, no. 3, pp. 3949–3967, 2022. [2](#)

[83] X. Huang, G. Mei, J. Zhang, and R. Abbas, "A comprehensive survey on point cloud registration," 2021. [Online]. Available: <https://arxiv.org/abs/2103.02690> [2](#)

[84] H. Lim, D. Kim, G. Shin, J. Shi, I. Vizzo, H. Myung, J. Park, and L. Carlone, "KISS-Matcher: Fast and robust point cloud registration revisited," in *IEEE Intl. Conf. on Robotics and Automation (ICRA)*, 2025. 3, 7, 12, 13

[85] R. Yao, S. Du, W. Cui, C. Tang, and C. Yang, "Pare-net: Position-aware rotation-equivariant networks for robust point cloud registration," in *European Conference on Computer Vision*. Springer, 2024, pp. 287–303. 3, 9, 10, 12

[86] C. Harris, M. Stephens *et al.*, "A combined corner and edge detector," in *Alvey vision conference*, 1988, pp. 10–5244. 3

[87] L. Sun and L. Deng, "TriVoC: Efficient voting-based consensus maximization for robust point cloud registration with extreme outlier ratios," *IEEE Robotics and Automation Letters*, vol. 7, no. 2, pp. 4654–4661, 2022. 3, 4, 5

[88] X. Zhang, L. Peng, W. Xu, and L. Kneip, "Accelerating globally optimal consensus maximization in geometric vision," *IEEE Transactions on Pattern Analysis and Machine Intelligence*, vol. 46, no. 6, pp. 4280–4297, 2024. 3, 4, 5

[89] S. S. Hansen, V. B. Ernstsen, M. S. Andersen, Z. Al-Hamdan, R. Baran, M. Niederwieser, F. Steinbacher, and A. Kroon, "Classification of boulders in coastal environments using random forest machine learning on topo-bathymetric LiDAR data," *Remote Sensing*, vol. 13, no. 20, p. 4101, 2021. 4

[90] E. Alexiou, X. Zhou, I. Viola, and P. Cesar, "PointPCA: Point cloud objective quality assessment using PCA-based descriptors," *EURASIP Journal on Image and Video Processing*, vol. 2024, no. 1, p. 20, 2024. 4, 5

[91] H. Lim, M. Oh, and H. Myung, "Patchwork: Concentric zone-based region-wise ground segmentation with ground likelihood estimation using a 3D LiDAR sensor," *IEEE Robotics and Automation Letters*, vol. 6, no. 4, pp. 6458–6465, 2021. 4, 5

[92] H. Yu, F. Li, M. Saleh, B. Busam, and S. Ilic, "CofiNet: reliable coarse-to-fine correspondences for robust pointcloud registration," *Advances in Neural Information Processing Systems*, vol. 34, pp. 23872–23884, 2021. 5

[93] D. Lowe, "Distinctive image features from scale-invariant keypoints," *Intl. J. of Computer Vision*, vol. 60, no. 2, pp. 91–110, 2004. 5

[94] J. E. Mebius, "Derivation of the Euler-Rodrigues formula for three-dimensional rotations from the general formula for four-dimensional rotations," *arXiv preprint math/0701759*, 2007. 5

[95] Z. Zhang, "Parameter estimation techniques: A tutorial with application to conic fitting," *Image and vision Computing*, vol. 15, no. 1, pp. 59–76, 1997. 6

[96] J. T. Barron, "A general and adaptive robust loss function," 2019. [Online]. Available: <https://arxiv.org/abs/1701.03077> 6

[97] P. Lindenberger, P.-E. Sarlin, and M. Pollefeys, "LightGlue: Local feature matching at light speed," in *Proceedings of the IEEE/CVF international conference on computer vision*, 2023, pp. 17627–17638. 6

[98] J. Shi, H. Yang, and L. Carlone, "ROBIN: a graph-theoretic approach to reject outliers in robust estimation using invariants," in *IEEE Intl. Conf. on Robotics and Automation (ICRA)*, 2021, arXiv preprint: 2011.03659, (pdf). 6, 7

[99] H. Yang, P. Antonante, V. Tzoumas, and L. Carlone, "Graduated non-convexity for robust spatial perception: From non-minimal solvers to global outlier rejection," *IEEE Robotics and Automation Letters (RA-L)*, vol. 5, no. 2, pp. 1127–1134, 2020. 7

[100] K. Ryu, S. Hwang, and J. Park, "Instant domain augmentation for lidar semantic segmentation," in *Proceedings of the IEEE/CVF Conference on Computer Vision and Pattern Recognition*, 2023, pp. 9350–9360. 7

[101] D. P. Kingma, "Adam: A method for stochastic optimization," *arXiv preprint arXiv:1412.6980*, 2014. 9

[102] R. Rusu, N. Blodow, and M. Beetz, "Fast point feature histograms (fpfh) for 3d registration," in *IEEE Intl. Conf. on Robotics and Automation (ICRA)*. Citeseer, 2009, pp. 3212–3217. 10, 12

[103] Y. Wang, H. Huang, C. Rudin, and Y. Shaposhnik, "Understanding how dimension reduction tools work: an empirical approach to deciphering t-SNE, UMAP, TriMAP, and PaCMAP for data visualization," *Journal of Machine Learning Research*, vol. 22, no. 201, pp. 1–73, 2021. 12

[104] L. v. d. Maaten and G. Hinton, "Visualizing data using t-SNE," *Journal of machine learning research*, vol. 9, no. Nov, pp. 2579–2605, 2008. 12

[105] H. Lim, D. Kim, and H. Myung, "Multi-Mapcher: Loop Closure Detection-Free Heterogeneous LiDAR Multi-Session SLAM Leveraging Outlier-Robust Registration for Autonomous Vehicles," *arXiv preprint arXiv:2511.00635*, 2025. 14

[106] F. Xia, A. R. Zamir, Z.-Y. He, A. Sax, J. Malik, and S. Savarese, "Gibson env: real-world perception for embodied agents," in *Computer Vision and Pattern Recognition (CVPR), 2018 IEEE Conference on*. IEEE, 2018. 14



Hyungtae Lim (Member, IEEE) received the B.S. degree in mechanical engineering, and M.S. and Ph.D. degrees in electrical engineering from the Korea Advanced Institute of Science and Technology (KAIST), Daejeon, Republic of Korea, in 2018, 2020, and 2023, respectively. He is currently a postdoctoral associate in the Laboratory for Information & Decision Systems (LIDS), Massachusetts Institute of Technology (MIT), Massachusetts, USA. His research interests include SLAM (simultaneous localization and mapping), 3D registration, 3D perception, long-term map management, spatial AI, and deep learning.



Minkyun Seo (Student Member, IEEE) received the B.S. degrees in Architectural Engineering and Computer Science and Engineering from Seoul National University (SNU), Seoul, Republic of Korea, in 2025, where he is currently pursuing the Ph.D. degree in Computer Science and Engineering through the integrated Ph.D. program. He is a member of the Visual and Geometric Intelligence Laboratory, advised by Prof. Jaesik Park. His research interests include 3D registration, 3D perception, and 3D reconstruction.



Luca Carlone (Senior Member, IEEE) received the B.S. degree in mechatronics from the Polytechnic University of Turin, Italy, in 2006, the S.M. degree in mechatronics from the Polytechnic University of Turin, Italy, in 2008, the S.M. degree in automation engineering from the Polytechnic University of Milan, Italy, in 2008, and the Ph.D. degree in robotics from the Polytechnic University of Turin, in 2012. He is currently the Leonardo career development associate professor with the Department of Aeronautics and Astronautics, the Massachusetts Institute of Technology, and a Principal Investigator in the Laboratory for Information & Decision Systems (LIDS). He joined LIDS as a postdoctoral associate (2015) and later as a research scientist (2016), after spending two years as a postdoctoral fellow with the Georgia Institute of Technology (2013–2015). His research interests include nonlinear estimation, numerical and distributed optimization, and probabilistic inference, applied to sensing, perception, and decision-making in single and multi-robot systems. His work includes seminal results on certifiably correct algorithms for localization and mapping, as well as approaches for visual-inertial navigation and distributed mapping.



Jaesik Park (Member, IEEE) received the bachelor's degree from Hanyang University in 2009, and the master's and Ph.D. degrees from KAIST in 2011 and 2015, respectively. He is an associate professor with the Department of Computer Science and Engineering, Seoul National University. He worked at Intel as a research scientist (2015-2019), and he was a faculty member at POSTECH (2019-2023). His research interests include image synthesis and 3D scene understanding.